

THESIS

THE DEVELOPMENT OF A THIN FILM SPUTTER DEPOSITION SYSTEM USING A  
NOVEL HIDDEN ANODE ION SOURCE AND MOTION CONTROL

Submitted by

Jack J. VanGemert

Department of Mechanical Engineering

In partial fulfillment of the requirements

For the Degree of Master of Science

Colorado State University

Fort Collins, Colorado

Spring 2020

Master's Committee:

Advisor: John D. Williams

Casey Farnell

Carmen Menoni

Jesse Wilson

Copyright by Jack J. VanGemert 2020

All Rights Reserved

## ABSTRACT

### THE DEVELOPMENT OF A THIN FILM SPUTTER DEPOSITION SYSTEM USING A NOVEL HIDDEN ANODE ION SOURCE AND MOTION CONTROL

Thin films consist of metallic or dielectric materials that are commonly deposited onto surfaces where properties, intrinsic to the thin film, are desired. Ranging from a single atomic layer to several microns in thickness, thin films are found to be useful for a broad range of applications. Most thin film applications desire uniform, durable, and adherent coatings with specific optical, electrical, or tribological properties. Therefore it is important that deposition systems can produce thin films with properties suited for the application at hand.

The development of a thin film sputter deposition system is presented. The system has been shown to produce large area art pieces at a low cost compared to current deposition systems. The deposition system uses a novel hidden anode ion source (HAIS) to sputter target material, assist film growth, and to clean substrates prior to deposition. To the author's knowledge, an ion source of this design has not been implemented in a deposition system prior to the one discussed. The characterization of a novel ion source is presented in detail along with the other system components. Deposition rates and thin film profiles are used to validate experimental results and predict thin film properties for various operating conditions. Coatings produced by the system are studied and used to determine film characteristics of interest to the application of outdoor art. Structural thin film properties of interest for long outdoor lifetime art work include film adhesion, density, and residual stress. Visual thin film properties important for the artwork are related to optical properties such as reflection, transmission, and absorption. The plasma-based deposition system is shown to be a tool of high potential for creating engaging, long lifetime art pieces.

## ACKNOWLEDGEMENTS

I would like to thank John Williams, Ryan Ham, Seth Thompson, and Plasma Controls for the assistance and support throughout the development of this project. I would also like to thank Carmen Menoni and her research team for the valuable conversations regarding thin film properties and measurement techniques.

## DEDICATION

*I would like to dedicate this thesis to Larry Bell for making this unique and exciting development project possible.*

## TABLE OF CONTENTS

ABSTRACT . . . . .	ii
ACKNOWLEDGEMENTS . . . . .	iii
DEDICATION . . . . .	iv
LIST OF TABLES . . . . .	vii
LIST OF FIGURES . . . . .	viii
Chapter 1	INTRODUCTION . . . . . 1
1.1	A Brief History . . . . . 2
1.2	Thin Film Growth . . . . . 2
1.2.1	Atomic Arrangement and Bonding . . . . . 2
1.2.2	Nucleation and Diffusion . . . . . 3
1.3	Kinetic Theory of Gases . . . . . 4
1.3.1	Molecular Flow . . . . . 4
1.3.2	Free Molecular Distribution . . . . . 6
1.3.3	Particle Flux . . . . . 8
1.4	Plasma Characteristics . . . . . 9
1.5	Sputter Deposition . . . . . 10
1.5.1	Ion Bombardment . . . . . 10
1.5.2	Reactive Sputtering . . . . . 12
1.5.3	Pulsed-DC Sputtering . . . . . 13
Chapter 2	VACUUM FACILITIES . . . . . 14
2.1	Facility 1: Gemini . . . . . 14
2.2	Facility 2: Howard . . . . . 15
Chapter 3	THE BIRTH OF A NOVEL ION SOURCE . . . . . 19
3.1	Iterations from Experimentation . . . . . 20
3.2	Ion Production Measurements and Results . . . . . 22
3.3	Sputter Deposition Proof of Concept . . . . . 25
Chapter 4	DEPOSITION SYSTEM COMPONENTS . . . . . 27
4.1	Hollow Cathode Electron Source . . . . . 27
4.2	Hidden Anode Ion Source . . . . . 29
4.3	Target Power Supply . . . . . 30
Chapter 5	DEPOSITION SYSTEM DEVELOPMENT . . . . . 33
5.1	Thin Film Profile Measurements . . . . . 33
5.2	Motion Testing for Thin Film Uniformity . . . . . 35
5.3	Ion Cleaning . . . . . 38
5.4	Motion Control . . . . . 40
5.5	System Assembly . . . . . 40
5.6	Gas Feed System . . . . . 40

Chapter 6	DEPOSITION SYSTEM CHARACTERIZATION . . . . .	43
6.1	Plasma Properties . . . . .	43
6.2	Ion Density Along Target Length . . . . .	47
6.3	Deposition Rates . . . . .	51
Chapter 7	THIN FILM CHARACTERIZATION . . . . .	56
7.1	Ellipsometry . . . . .	56
7.2	Residual Stress . . . . .	58
Chapter 8	DISCUSSION . . . . .	61
8.1	Substrate Cleanliness . . . . .	61
8.2	System Scaling . . . . .	62
Chapter 9	CONCLUSION . . . . .	64
Bibliography	. . . . .	65
Appendix A	Alumina Silicate Curing Procedure . . . . .	70
Appendix B	Motion Control Sample Program . . . . .	71
Appendix C	Needle Valve Mass Flow Rate Settings for Argon . . . . .	79
Appendix D	Bill of Materials . . . . .	80
Appendix E	Flux Calculations for Desired Thin Film Stoichiometry . . . . .	82

## LIST OF TABLES

2.1	Pump speeds for Gemini . . . . .	15
2.2	Pump speeds for Howard . . . . .	16
5.1	Deposition results for various target lengths . . . . .	33
6.1	Indicated and measured ion current to target surface comparison . . . . .	51
7.1	Percent porosity comparison for HAIS deposited thin films and other TiO <sub>2</sub> materials . .	58

## LIST OF FIGURES

1.1	Thornton structure zone model for temperature and pressure effects on thin film structure	4
1.2	Maxwell-Boltzmann speed distribution for argon . . . . .	7
1.3	Maxwell-Boltzmann energy distribution for argon . . . . .	8
1.4	Possible events caused by particle bombardment on a target surface . . . . .	10
1.5	Sputter yield versus argon ion energy . . . . .	11
2.1	Schematic of Gemini . . . . .	15
2.2	Photo of Gemini . . . . .	16
2.3	Chamber pressure as a function of mass flow rates of Ar, N <sub>2</sub> , and O <sub>2</sub> for the 1,200 L facility . . . . .	17
2.4	Photo of Howard . . . . .	17
2.5	Chamber pressure as a function of mass flow rate of Ar, N <sub>2</sub> , and O <sub>2</sub> for the 5,000 L facility . . . . .	18
3.1	Cross-sectional schematic of the hidden anode device . . . . .	19
3.2	Cross-sectional schematic of early hidden anode design . . . . .	20
3.3	Operating temperatures near hidden anode orifice for discharge current and gas flow operating conditions . . . . .	21
3.4	Hidden anode ion current saturation for ion production measurements . . . . .	23
3.5	Ion production current as a function of anode discharge current and Ar flow rate . . . . .	23
3.6	Hidden anode ion production as a function of discharge power for various argon flow rates . . . . .	24
3.7	Hidden anode discharge voltage as a function of anode discharge current and Ar flow rate . . . . .	25
3.8	Photo of early sputter deposition testing with titanium electrode plate . . . . .	26
4.1	Photo of the deposition system components assembled on a mounting block . . . . .	27
4.2	Cross-sectional schematic of cathode assembly . . . . .	28
4.3	Photo of disassembled hollow cathode components . . . . .	29
4.4	Cross-sectional schematic of hidden anode ion source . . . . .	30
4.5	Photo of hidden anode fully assembled . . . . .	31
4.6	Electrical schematic of the plasma circuit during deposition . . . . .	32
5.1	Photo of experimental setup for stationary thin film thickness profile experiments using a tubular target for deposition . . . . .	34
5.2	Thickness profile for Ti and TiO <sub>2</sub> coating on glass substrates . . . . .	35
5.3	Measured thickness profile and summed profiles for modelled thickness uniformity . . . . .	36
5.4	Thin film surface generated from measured thickness over substrate area post deposition . . . . .	37
5.5	Photo of deposition results from substrate cleanliness testing . . . . .	39
5.6	Photo of deposition during motion testing . . . . .	39
5.7	Photo of deposition system assembled on a two axis motion system . . . . .	41
5.8	Gas feed system schematic for cathode and hidden anode plasma devices . . . . .	42

6.1	Triple probe electrical schematic . . . . .	44
6.2	Electron temperature versus target bias for various anode discharge currents . . . . .	45
6.3	Electron density versus target bias for various anode discharge currents . . . . .	46
6.4	Photo of experimental setup for Faraday probe measurements . . . . .	48
6.5	Ion current density with and with out biased target over length of target . . . . .	49
6.6	Ion current density and ion density along target length for various anode discharge currents . . . . .	50
6.7	Deposition rate versus increasing and decreasing process gas flow rate . . . . .	52
6.8	Deposition profile for various target biases and process gas species at a 20cm throw distance . . . . .	54
6.9	Deposition profile for various target biases and process gas species at a 12.5cm throw distance . . . . .	55
7.1	Bulk rutile TiO <sub>2</sub> refractive index comparison to TiO <sub>2</sub> thin films prepared by HAIS deposition system . . . . .	57
7.2	Radius curvature contour plot of TiO <sub>2</sub> thin film and interference signal used for residual stress measurement . . . . .	60

# Chapter 1

## INTRODUCTION

This thesis traverses a timeline that covers the development of a thin film deposition system used for creating visual art. The project started with the conceived idea of a ‘hidden’ anode plasma device, which was found to be a useful tool for depositing thin films. Discoveries about the device were made through experimentation, such as the rate of ion production, the ease of manufacturing, the flexibility in design, and the low costs related to device fabrication and operation. These findings gave rise to exploring the potential uses of the hidden anode, specifically for a thin film deposition application. A proof of concept for a biased target sputter coating system is shown to be capable of depositing adherent thin films onto glass at relatively high deposition rates. The development of this coating system was pursued with the goal of producing visually interesting thin films that may require lifetime enhancing properties for outdoor environments. The term ‘visually interesting’ is used to describe the goal of the artwork, meaning the viewer will be pulled into looking at and experiencing the piece more in depth by means of curiosity or interest.

Before diving into the details of the deposition system, the background and physics related to the thin films will be briefly covered. This will help aid any reader in understanding the topics discussed within the thesis, as well as providing helpful resources related to these topics.

## **1.1 A Brief History**

Thin film usage dates back to over 5,000 years ago, where precious items were coated in gold for preservative and decorative purposes [1]. Although these ancient methods for creating thin films are much different than what is commonly used today, it is interesting to note the prominence thin films have had on many separate cultures throughout history. It wasn't until the enhancements in vacuum technologies in the 1800's that made thin films popular in our modern society. They are used for numerous applications such as protective coatings, optical filters, semiconductor devices, visual decor, and more [2].

## **1.2 Thin Film Growth**

Atomic structures and bonds, inherent to materials, grant various material properties [3]. When a material is used for an application, it is chosen based on the properties inherent to that material. Therefore when working with thin films, it is beneficial to understand what material properties result from certain atomic arrangements, and how the desired arrangements can be produced.

### **1.2.1 Atomic Arrangement and Bonding**

Atoms can be arranged in a crystal structure, or a random, amorphous structure. Due to the atomic arrangement, different material properties are observed. Various electrical, optical, and mechanical properties will be observed based on these structural changes at the atomic level. For example, if an iridescent thin film is desired on a smooth glass surface, a polycrystalline thin film can be deposited in a manner that produces columnar grain growth at some angle normal to the glass surface. For various observation angles' there will be different colors observed, which result from the anisotropic atomic arrangement [4,5].

Within these atomic structures, there can be different types of bonds that hold the atoms in place, and in effect, determine material properties. Common day materials, such as aluminum foil or glass, are observed to have specific properties that result from the atomic bonds within the material. Aluminum foil compared to glass for example, is reflective but not transparent to visible light,

while glass is reflective and transparent in this same visible spectrum. These observations have been shown to be due to the bonds associated with these two different materials. The difference in bonds affect the motion of light, or photons, in three different ways; through reflection, transmission, and absorption [3, 5, 6]. These quantifiable properties can be used to describe both solid bulk materials and thin films. For the application at hand, thin film material properties are chosen to enhance outdoor lifetime, as well as provide the optical characteristics which affect the incident light. Extensive details regarding material science will not be discussed here. Instead the topics are mentioned as a starting point for considering what types of arrangements and bonds are needed to provide a desired property. These topics have been thoroughly covered in several resources written over the years, and they are an excellent resource for learning more about the topics [3, 6].<sup>1</sup>

## **1.2.2 Nucleation and Diffusion**

Desired atomic arrangements in a thin film can be achieved early in the growth process, during deposition, or even after thin film deposition. Nucleation describes the formation site of an atomic structure in a material phase and is the first step in thin film growth. As thin films are deposited, nucleation sites can form on a substrate that allow for crystal growth to occur. During the deposition process, thin film properties can be altered by means of interatomic diffusion. By allowing bonds to weaken and atoms to move within the thin film, the atomic structure will also change, thus altering film properties. Another way that material structures can be altered is after thin film deposition by annealing processes. All of these processes mentioned can be controlled by energy and temperature input to the film [3, 6]. The well-known Thornton structure zone model, shown in Figure 1.1, is used to describe how temperature and pressure have a direct effect on the atomic structure of a thin film during deposition. This model is accurate for temperature effects, but does not take into account the effect that additional energy has on the thin film, which has also been shown to have strong influence on film structure. Specifically momentum and energy have been shown to enhance interatomic diffusion by means of atomic peening. This technique has been

---

<sup>1</sup>For more info on the material science related to the topic of thin films see references [6, 7].

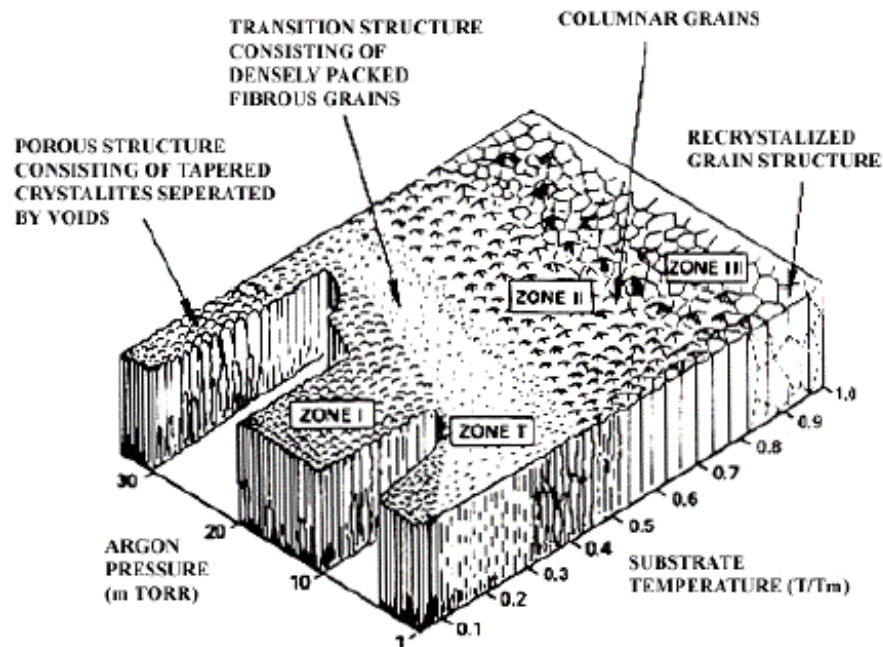


**Figure 1.1:** Thornton's zone model for temperature and pressure effects on thin film structure. Adapted from "Influence of Processing Variables on the Properties of DC magnetron Sputtered NiAl Coatings Containing Hf Additions," by B. Ning et al, 2005, *Journal of Vacuum Science and Technology, A*, p. 43. Copyright [2005] by the American Vacuum Society [8].

shown to affect mechanical properties like density and stress of thin films during deposition. Stress is an important mechanical material property to consider for outdoor thin film applications because it can be used to indicate thin film density. Thin films will survive longer if they are dense, and by changing the energy and temperature to the film during or after deposition, a desired film density can be achieved [9, 10].

## 1.3 Kinetic Theory of Gases

### 1.3.1 Molecular Flow

A low pressure environment is needed to grow thin films using physical vapor deposition (PVD) techniques. This becomes evident when considering the relationship between pressure and density. By decreasing pressure, the number of particles in a volume decreases, which is shown by the ideal gas law. When the number of particles occupying a volume decreases, the particles in the

volume can travel longer distances before colliding with one another on average. In other words, the probability of particles colliding decreases with decreased particle density. This is useful for PVD techniques, such as thermal evaporation and sputtering, because the particles composing the film need to travel long distances (compared to their size) before colliding and condensing on the desired surface, or substrate. This average distance is defined as the mean free path,  $\lambda_{\text{mfp}}$ , and is shown in equation (1.1) [6, 7, 11, 12].

$$\lambda_{\text{mfp}} = \frac{1}{\sqrt{2}n\sigma}, \quad (1.1)$$

Where  $n$  is the density of particles and  $\sigma$  is the collisional cross-section of the gaseous particles within the system.<sup>2</sup>

It can be shown with the ideal gas law that the system pressure has a direct influence on the density of molecules in the system for a fixed volume and temperature. Due to the inverse relationship between the mean free path and density,  $n$ , the mean free path increases with decreasing pressure. As the mean free path increases and collisional events decrease, the behavior of particles in the system changes. Different flow regimes are used to describe the behavior of molecules within these different environments. The Knudsen number, which is a ratio of a characteristic length and the mean free path, is the parameter used to determine the flow regime in a control volume [6, 7, 11, 14]. The Knudsen number is shown in equation (1.2).

$$\mathbf{Kn} = \frac{L_c}{\lambda_{\text{mfp}}}, \quad (1.2)$$

Where  $L_c$  is the characteristic length of the control volume considered. The minimum distance vapor particles are desired to travel should be used for this length to ensure successful film growth [11]. The flow regimes are defined below by the ranges of Knudsen numbers.

---

<sup>2</sup>For more information about collisional cross-sections see references [7, 13].

$$\left\{ \begin{array}{ll} \text{free molecular flow} & \mathbf{Kn} < 1 \\ \text{intermediate flow} & 1 < \mathbf{Kn} < 110 \\ \text{viscous flow} & \mathbf{Kn} > 110 \end{array} \right.$$

At small mean free paths, for example in a pool of water, molecules chaotically collide with one another at such high rates that it is simple to describe the bulk media as a continuum of packed molecules that obey Newtonian-type physical laws. Contrary to the viscous flow regime, at large mean free paths, molecules travel freely and collisional rates are low. The free molecular flow regime is desired for thin film growth due to the low collisional rates among particles. More vapor particles are able to maintain initial velocities and energies at lower collision rates, which, as mentioned previously, can be useful for controlling nucleation and diffusion processes. Due to the requirement of a low pressure environment, a vacuum facility is a common component among thin film deposition systems. In the free molecular flow regime, several assumptions can be made to describe the molecules in the system.

### 1.3.2 Free Molecular Distribution

In the free molecular flow regime, where  $\mathbf{Kn} < 1$ , molecules can be described by probability distributions, which can be convenient for describing the state of a control volume. In order to do this, some assumptions are made. It can be assumed that the molecules in the free molecular flow regime are in continuous random motion, and completely dependent on the temperature of the gas. The ideal gas law approximation says there are no interatomic forces between particles, and that the only means for transferring kinetic energy is through elastic collisions, which leads to a steady-state distribution of molecular velocities in the volume [6, 13, 15]. After making these assumptions, the gaseous particles can be described by the Maxwell-Boltzmann distribution function,  $f(v)$ , as shown in equation (1.3).

$$f(v) = \frac{1}{n} \frac{dn}{dv} = \frac{4}{\sqrt{\pi}} \left| \frac{M}{2RT} \right|^{3/2} v^2 \exp\left[-\frac{Mv^2}{2RT}\right], \quad (1.3)$$

Where  $M$  is the molar mass of the gas species,  $v$  is the velocity of the gas molecule,  $R$  is the ideal gas constant, and  $T$  is the temperature of the gas. This distribution is shown in Figure 1.2 for a visual representation of the dependence between molecular velocities and the temperature of the system. With this distribution function, the velocity of gaseous particles can be described purely

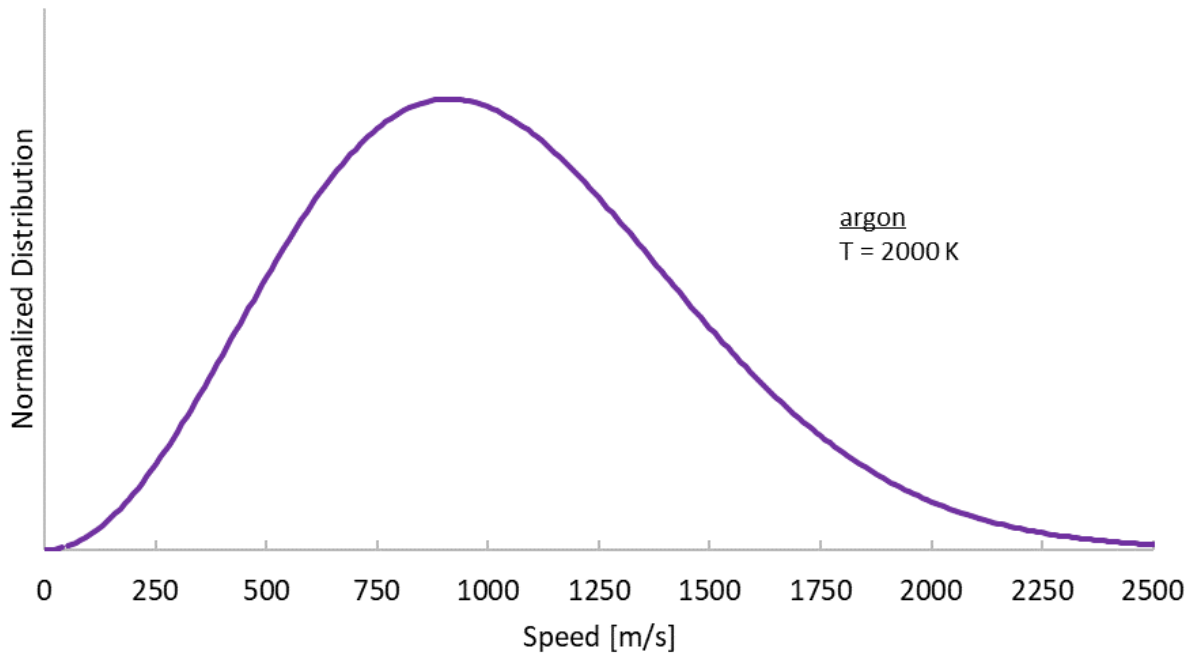


**Figure 1.2:** Maxwell-Boltzmann speed distribution for argon.

by their temperature and gas species. Since the temperature of the gas can be used to describe the probable speed, it can also be used to describe the kinetic energy of the system [12]. Consider the familiar equation for kinetic energy shown in equation (1.4).

$$K.E. = \frac{1}{2}mv^2, \quad (1.4)$$

This relation leads to the Maxwell-Boltzmann distribution that describes the energy distribution of the system. Figure 1.3 provides a visual for how the temperature of the gas species can be used to

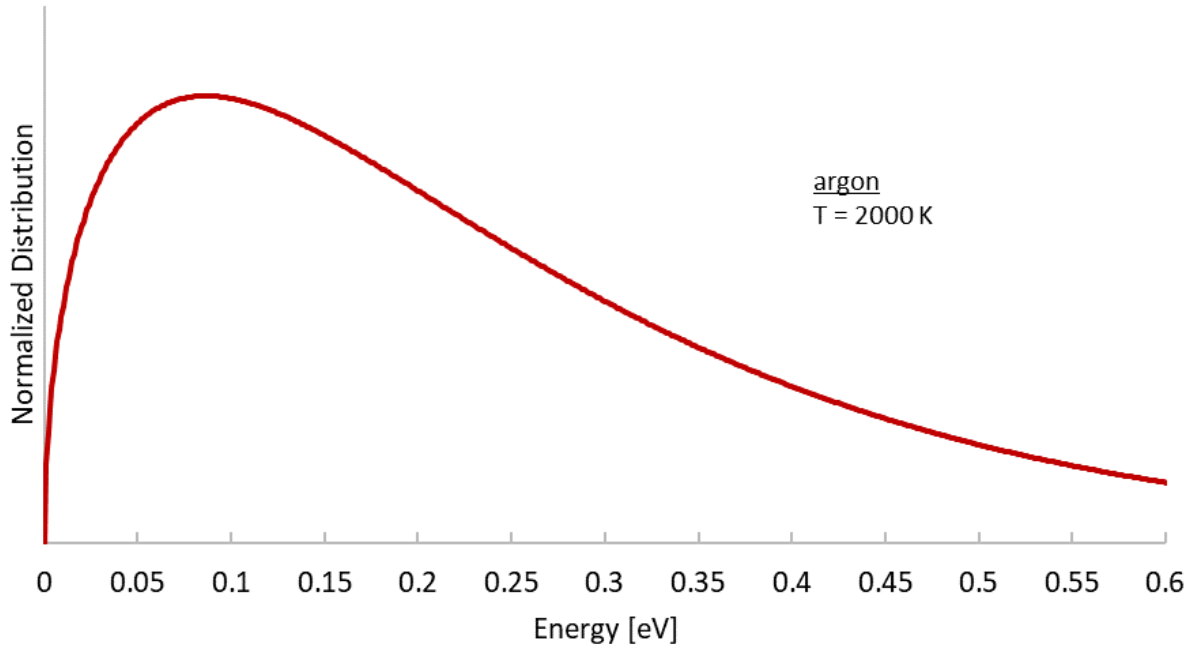


**Figure 1.3:** Maxwell-Boltzmann energy distribution for argon.

describe the energy of the system. These distributions allow for important plasma properties in the system to be acquired, which are used to describe the deposition process later.<sup>3</sup>

### 1.3.3 Particle Flux

It is useful to have an expression that describes the flux of particles to a substrate surface when growing thin films. This is important for determining how quickly the substrate will be coated with a desired material or an undesired, contaminant material. The particle flux, or the number of gas molecules impinging a surface per unit time and area is shown in equation (1.5).

$$\Gamma = n\sqrt{\frac{RT}{2\pi M}}, \quad (1.5)$$

Where  $\Gamma$  is the particle flux,  $n$  is the density of molecules,  $R$  is the ideal gas constant, and  $T$  is the temperature of the gas. For convenience, particle flux can be expressed in terms of Torr, a common

---

<sup>3</sup>For more details related to the physics used to describe free molecular flow see references [6, 13–15].

unit for pressure. This conversion of equation (1.5) is shown in equation (1.6).

$$\Gamma = 3.513 \times 10^{22} \frac{P}{\sqrt{MT}}, \quad (1.6)$$

Where  $T$  and  $P$  are in units of Kelvin and Torr, respectively. Another useful factor to consider is the time it takes for a monolayer of gas to form on a substrate surface. To enhance thin film adhesion on the substrate, a clean substrate surface is required prior to deposition. The time it takes for a monolayer of gas to form on a surface is shown in equation (1.7).

$$\tau = \frac{10^{15}}{3.513 \times 10^{22}} \frac{\sqrt{MT}}{P}, \quad (1.7)$$

Where  $T$  and  $P$  are in units of Kelvin and Torr, respectively. At standard temperature and pressure, a monolayer will form in less than 1 nanosecond, and at pressures of  $1 \times 10^{-3}$  Torr a layer will form in 1 second. For good film adhesion, it is required that thin film growth must occur faster than the flux of contaminants to the surface after it is cleaned [6, 7, 11, 15].

## 1.4 Plasma Characteristics

A plasma is defined as a disassociated gaseous material consisting of neutral gas species, ions, and electrons that averages a net charge of zero when considering all the particles within it [6, 14]. It is important to consider how a plasma interacts with a surface in order to understand how sputtering occurs, as well as how plasma properties can be measured. The mass of an electron is five orders of magnitude less than the mass of an ion or neutral atom. Due to this mass difference, there is a large difference in mobility among the particles within the plasma. Since electrons travel much quicker than ions, any surface that is immersed in a plasma will be suddenly covered in electrons, resulting in the surface to quickly ‘float’ at a negative potential, relative to the bulk plasma [14]. This negative surface charge causes ions to accelerate towards the surface. Due to the ions response to the negative potential, a quasi-neutral sheath is formed between the bulk plasma and the negative surface, where the density of ions and electrons are not equal. Ions with enough

kinetic energy, determined by the negative bias of the surface, will penetrate the surface [14]. When an ion penetrates a surface, a number of events could occur, such as sputtering [6].

## 1.5 Sputter Deposition

### 1.5.1 Ion Bombardment

Sputtering is a common PVD technique for growing thin films. Sputtering occurs when particles are accelerated towards a target surface with enough energy and momentum to dislodge, or sputter, the target atoms from the surface and subsurface region. Due to several factors, numerous events can occur at the target surface during the bombardment of ions. The factors are ion energy, ion species, ion angle of incidence on the target surface, the target species, and the target surface and subsurface atomic structure. These factors determine what events happen in this process, which are described in Figure 1.4 [6].

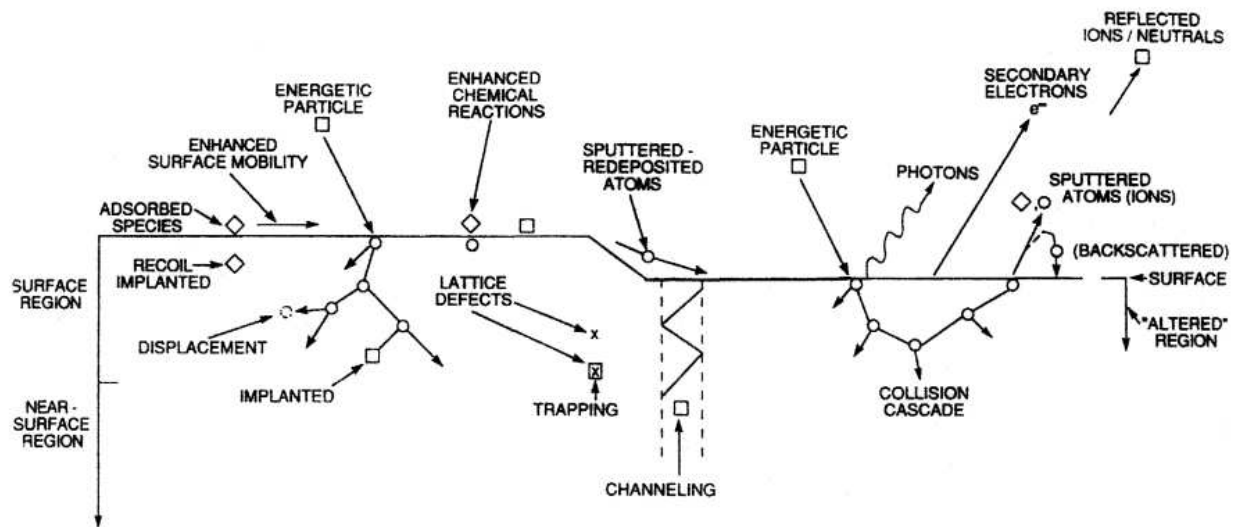


**Figure 1.4:** Possible results caused by particle bombardment on a target surface. Adapted from "*Materials Science of Thin Films*" (p. 171), by M. Ohring, 2001, Academic Press 2nd edition. Copyright 2001 Academic Press [6].

Many of these events that occur during sputter deposition are not desired, and may be considered losses in energy. A term, known as the sputter yield, is used to quantify the effectiveness

of sputtering. The sputter yield is defined as the number of atoms sputtered from a target surface per incident ion. The sputter yield can be optimized by considering the kinetic energy of ions and the momentum exchange between ions and target atoms. The sputter yield is shown graphically for various target materials at different ion energies in Figure 1.5 [16]. As shown in Figure 1.5, a

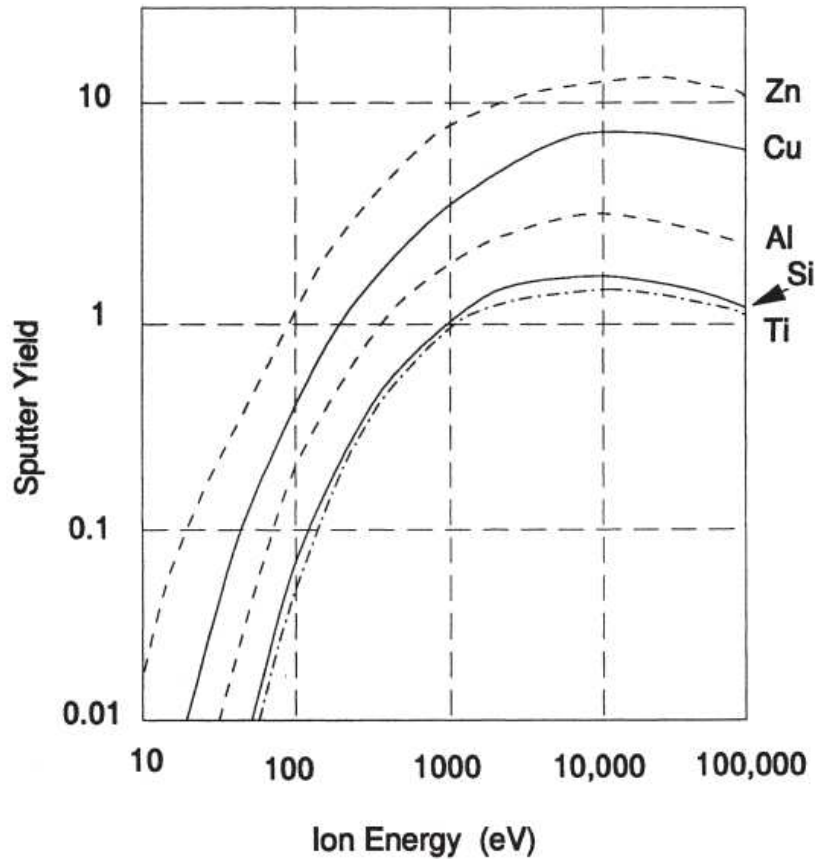


**Figure 1.5:** Sputter yield versus argon ion energy. Adapted from "*Handbook of Thin Film Deposition Processes and Techniques*"(p.322), by K. Seshan, 2002, Noyes Publications. Copyright 2002 Noyes Publications [16].

maximum sputter yield is observed experimentally, which is determined by the factors previously mentioned [6, 16, 17]. The kinetic energy of the impacting ion needs to be large enough to overcome the binding energy of the target atoms to successfully sputter target atoms. At too low of energy, the ion will not have enough energy to sputter, and will likely be reflected from the target surface as either a neutral or ion. At too high of energy, the ion will implant into the target surface.

There is a range of energy at which ions will transfer a sufficient amount of energy to sputter target material. The momentum exchange between ion and target atoms can be maximized to increase sputter yield by matching the size and mass of the incident ion and target atom [6].

Another important factor known as the deposition rate is used to evaluate a deposition process. It is defined as the rate of change in thickness over time, commonly expressed in units of nanometers per minute or angstroms per second. It is a useful parameter for determining how long a deposition should last for a desired film thickness. Deposition rates are material specific and can be determined experimentally through several measurement techniques. For the deposition system considered here, deposition rates were found for titanium and copper targets at several operating conditions of interest.

A specific sputter deposition technique is used for this application, where ions are accelerated through an electric potential near the target surface. This is done by applying a negative bias on a metallic target. This bias determines the kinetic energy and momentum at which the ions impinge the surface. It is common to apply a DC bias on a metallic target to grow metallic thin films. Sometimes other bias methods are used when there is process gas present in the deposition environment, known as reactive sputtering.

### **1.5.2 Reactive Sputtering**

Reactive sputtering is a technique used to grow thin films consisting of dielectric compounds such as oxides, carbides, nitrides, sulfides, or combinations of these. During reactive sputtering, process gas can be introduced into the background environment to cause chemical reactions with the sputtered metallic target material. Depending on the sputter rate and the flux of process gas introduced during deposition, there can be many stoichiometric outcomes, and as a result, produce different thin film properties [6, 11]. This process can be accomplished through several techniques, but it is of interest here to discuss two techniques: DC sputtering and pulsed-DC sputtering.

### **1.5.3 Pulsed-DC Sputtering**

Pulsed-DC sputtering, as the name tells, uses a time series of DC pulses to sputter the target. This sputtering technique is typically desired for reactive sputtering applications. During reactive sputtering, a dielectric layer can form on a metallic target through chemical reactions. When these layers form, a target is considered to be poisoned, meaning the purity of the metallic target has decreased. Dielectric contaminants on the metallic target surface float at an electric potential different than the bias applied to the target, and may lead to arcs due to the immobility of electrons in the dielectric. By pulsing the target, the metallic target could clean itself from gas contaminants and charge build-up, leading to a more effective deposition process. By pulsing the target in the 10 - 350kHz range with 50 - 90% duty cycles, arcs can be eliminated due to the high mobility of electrons compared to ions in the plasma. Between negative pulses, the target surface pulses positive, and electrons in the plasma rush to the target to clean the surface of charge build up and of contaminants by means of heat [18]. By pulsing the target, ionization events could also be enhanced during deposition, which leads to an increase in ion density [19]. This could be useful for enhancing diffusion within the film, as well as increase deposition rates.

## Chapter 2

# VACUUM FACILITIES

Two different vacuum facilities, located at Colorado State's CEPPE Lab, were used during the development of the deposition system. The first facility, a vacuum chamber owned by Plasma Controls LLC, was used for the majority of preliminary experiments and proof of concept testing. The second facility described in this chapter is much larger than the first facility, and it is equipped with a diffusion pump. It is a vacuum chamber owned by Colorado State University's CEPPE Lab, and is more true to the vacuum facility that will house the final deposition system in Larry Bell's studio. Therefore, it was important to gather a qualitative understanding of whether or not the diffusion pump oil has an affect on thin film adhesion or substrate cleanliness. The pump speeds were found for each facility to gather an understanding of how much gas flow throughput the pumps could handle. Prior to testing, the facilities were leak checked using a residual gas analyser (RGA) to ensure a leak tight system during experimentation. It was also pumped to a base pressure of  $10^{-6}$  Torr prior to deposition to limit the level of contaminants in the system such as water and oils [20].

### 2.1 Facility 1: Gemini

Gemini is a 1,200 liter cylindrical tank equipped with a mechanical roughing/backing pump and a turbo-molecular hi-vac pump. The mechanical pump was used to reduce the pressure of the facility and the foreline to a rough vacuum of approximately 200mTorr, a pressure adequate for safe turbo pump operation. The roughing valve was then closed, and the foreline was opened. The facility was then brought to high vacuum by opening the gate valve to allow for the turbo pump to operate. A schematic of the vacuum facility and pump train is shown in Figure 2.1. A photo of the facility is also shown in Figure 2.2.

The pump speed of the system was calculated for several gas species of interest, and the data are tabulated in Table 2.1.

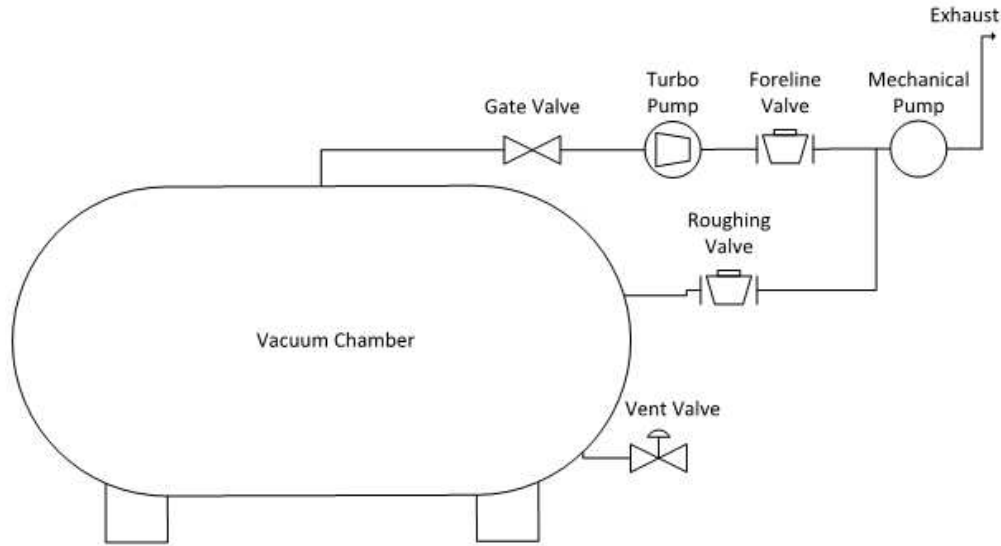


**Figure 2.1:** Schematic of vacuum Gemini.

**Table 2.1:** Pump speeds for Gemini.

Pump Speed [L/s]	Gas Species
1,422	Ar
2.170	N <sub>2</sub>
1,854	O <sub>2</sub>

The pump speeds were found by plotting the linear relationship between the chamber pressure indicated by a calibrated ion gauge at known mass flow rates using a calibrated mass flow controller. By modifying the units for mass flow rate, given in sccm, to Torr L/s, the pump speed can be found by taking the inverse slope of the line. Figure 2.3 shows the linear relationship between mass flow rate and pressure.

## 2.2 Facility 2: Howard

The second vacuum facility, Howard, is a 5,000 liter cylindrical tank which is equipped with a mechanical roughing/backing pump and a diffusion pump. A photo of the vacuum facility is shown in Figure 2.4. Between the diffusion pump and the vacuum chamber, an optically dense baffle was used to limit the amount of diffusion pump oil contamination introduced into the system during

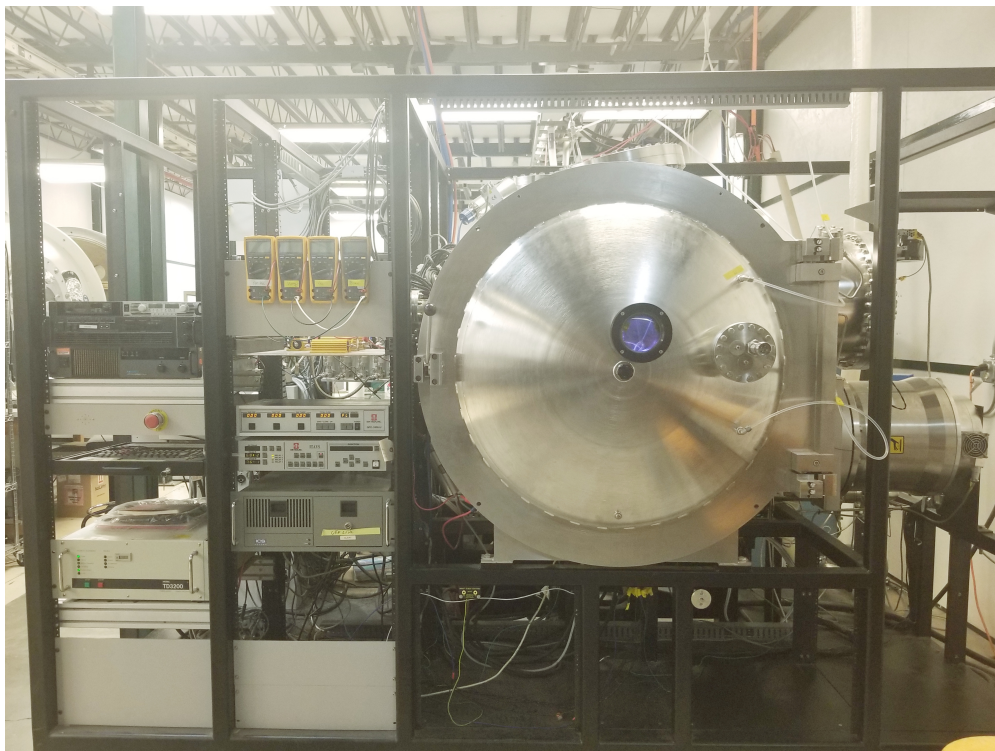


**Figure 2.2:** Photo of Gemini.

testing. The pump speeds for this facility were also calculated for the gas species of interest, and the data are shown in Table 2.2.

**Table 2.2:** Pump speeds for Howard.

Pump Speed [L/s]	Gas Species
11,066	Ar
16,133	N <sub>2</sub>
14,932	O <sub>2</sub>

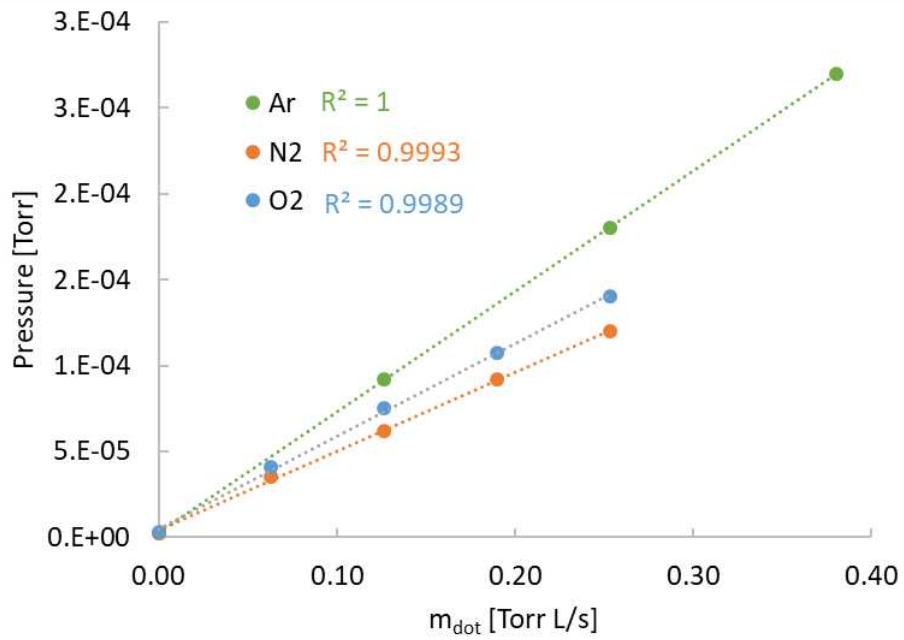


**Figure 2.3:** Chamber pressure as a function of mass flow rates of Ar, N<sub>2</sub>, and O<sub>2</sub> for the 1,200L facility.

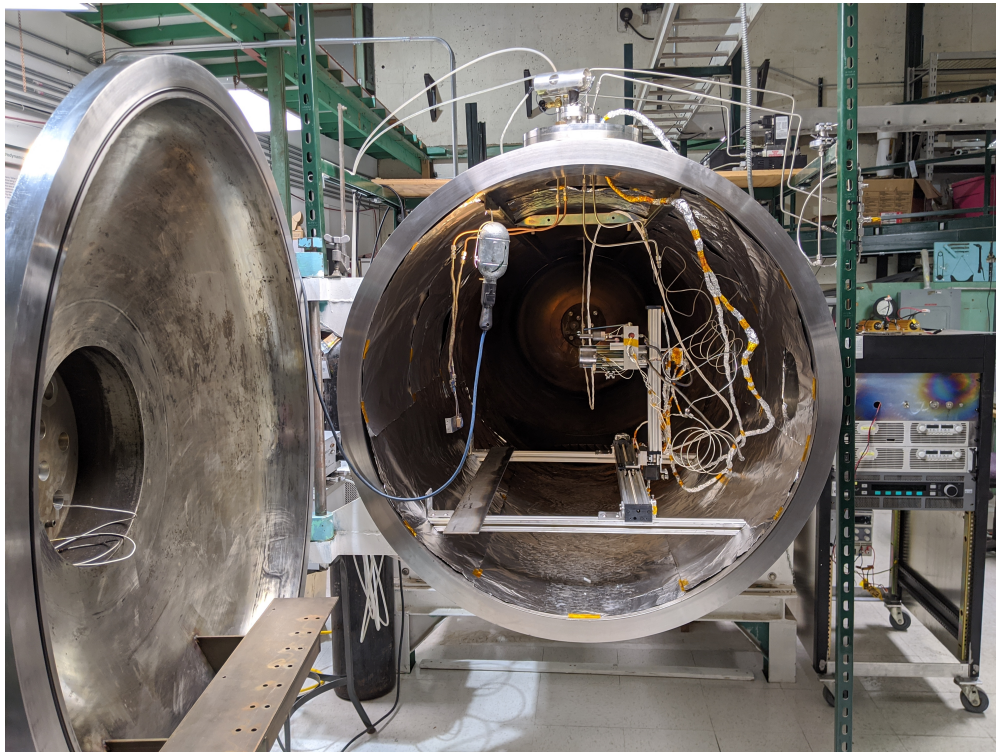


**Figure 2.4:** Photo of Howard.

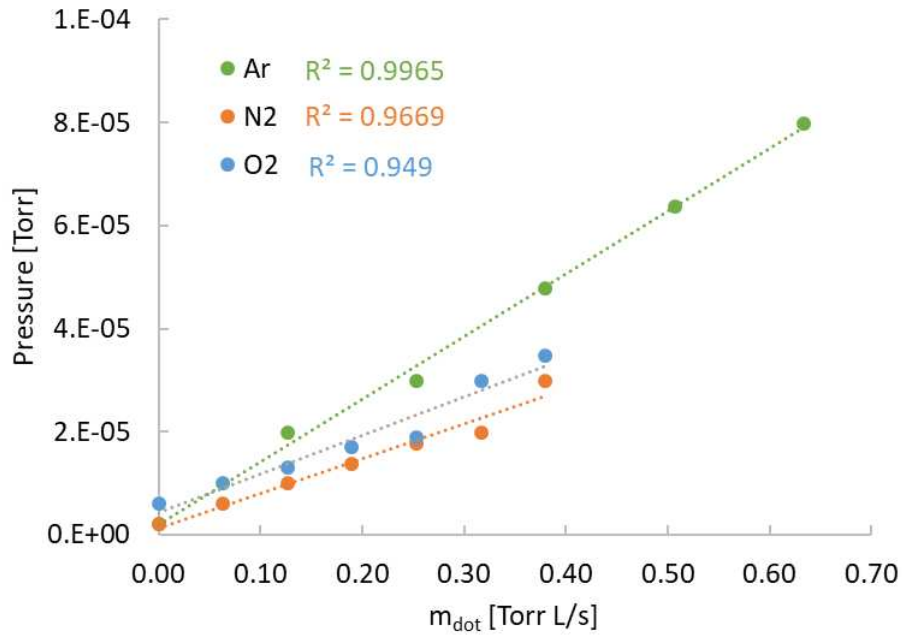


**Figure 2.5:** Chamber pressure as a function of mass flow rate of Ar, N<sub>2</sub>, and O<sub>2</sub> for the 5,000L facility.

## Chapter 3

### THE BIRTH OF A NOVEL ION SOURCE

The idea behind the hidden anode device is to produce ions through collisional events among electrons and argon gas molecules. This is done by flowing electrons into a dense volume of neutral argon atoms from a low pressure plasma discharge. The idea was conceived by Vladimir Gorokhovskiy, and physically developed and studied at Colorado State University's CEPPE Lab [21,22]. A design of the hidden anode is shown in the cross-sectional view in Figure 3.1.

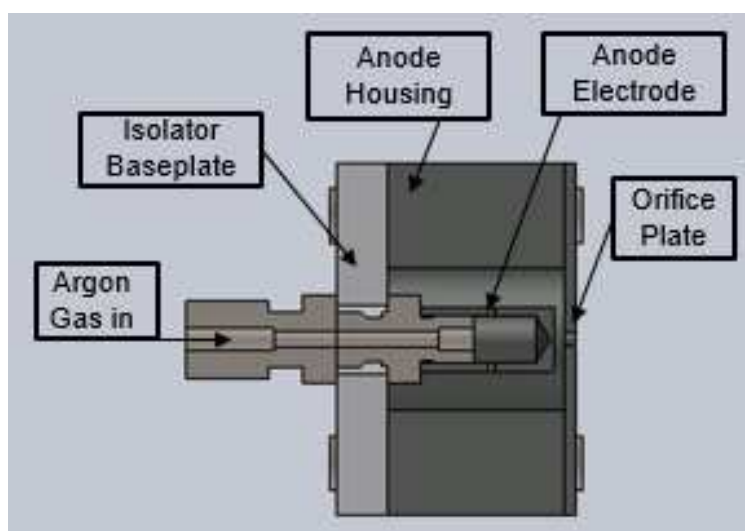


**Figure 3.1:** A cross-sectional schematic of the hidden anode device.

When considering the device design, specifically the enclosed anode electrode, the origin of the name 'hidden anode' becomes obvious. The design calls for electrically conductive materials for electrodes and insulative materials for isolating electrodes. The device needs to have an inlet for gas flow, and an orifice for ion/neutral out-flow and electron in-flow. The final requirement is to house the anode electrode inside the device. This isolation is crucial for ion production, as it will only allow electrons to travel through the orifice plate. The positive lead of a DC power supply is connected to the anode and the negative lead is held at cathode potential, where the electrons

are supplied. If all the criteria are met, then the hidden anode device can be made to operate successfully.

### 3.1 Iterations from Experimentation

Many design changes resulted from experimenting with device materials. Although many experiments lead to unexpected outcomes, valuable things were learned and used to optimize the device. Early designs of the hidden anode were made using a stainless steel body and a graphite orifice disk that enclosed an isolated tubular tantalum anode. This early design was inspired by a the design of a heaterless hollow cathode by Plasma Controls, and is shown in Figure 3.2.

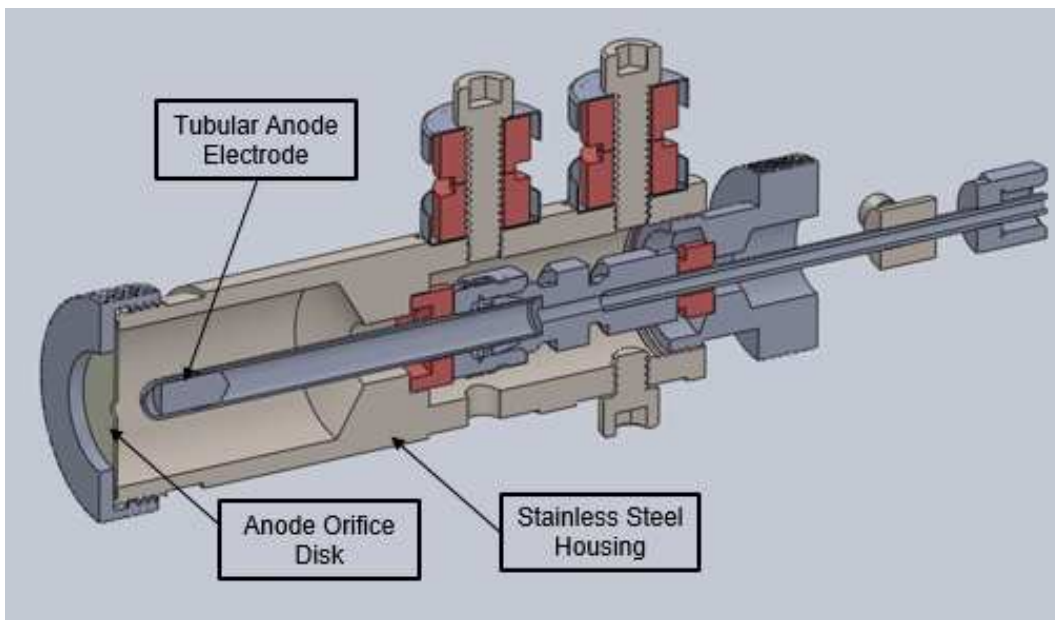


**Figure 3.2:** Cross-sectional schematic of early hidden anode design. Adapted from Plasma Controls HCES hollow cathode design.

Initial tests quickly revealed the difficulty in starting the hidden anode. While trying to couple the cathode to anode, electrode decoupling was observed. It was found that to start the device successfully, large anode flow rates were needed to successfully couple electrons through the orifice.

After testing the device operation with the design shown in Figure 3.2, it was revealed that the tantalum tube was not able to withstand the high temperatures during operation. The refractory

metal melted at the tip, near the orifice plate. It became evident that a lot of energy was going into the device and even high temperature materials such as refractory Ta cannot be used for long periods of time. Due to this finding, graphite was elected as a candidate for anode material due to the electrical properties and extremely high melting point of graphite. A graphite tube with similar dimensions as the Ta tube was machined from cylindrical stock and replaced the Ta tube shown in Figure 3.2. The new anode material proved to withstand the same checkout testing as the first design, and lead to an attempt to characterize the device.

After melting the refractory tube, it was natural to wonder what the device's temperatures were during operation. A pyrometer was employed in an experiment that measured the temperature of the anode at several operating conditions. Temperature data for the hidden anode were found by flowing current through the pyrometer's filament to match the emission color with the plasma in the orifice by aligning the pyrometer lens at a view port outside of the vacuum chamber. Figure 3.3 shows the temperature measurements for various discharge currents and argon flow rates. The temperature was found to be less than the sublimation temperature of tantalum ( $3,000^{\circ}\text{C}$ ) at

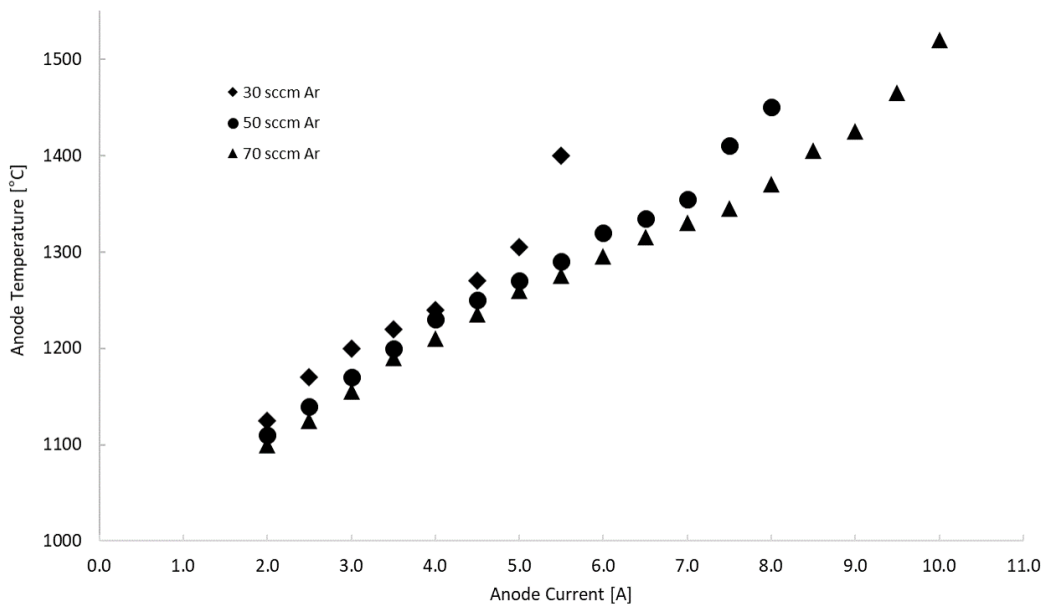


**Figure 3.3:** Operating temperatures near hidden anode orifice for discharge current and gas flow operating conditions.

pressures near  $10^{-2}$  Torr for all conditions [23]. This suggested that the measured temperature was not representative of the anode's temperature inside the device, but likely the representative of the dense plasma's temperature near the orifice. The plasma is likely blocking sight of the anode electrode during operation. The device entered unstable operating conditions where these data began approaching a vertical asymptotic behavior. After testing the device operation and start up procedure, the level of ion production was determined.

## 3.2 Ion Production Measurements and Results

Experiments were conducted to determine the level of ion production, as well as to characterize nominal operating conditions. A hidden anode device equipped with a graphite anode and a graphite orifice plate of 0.055" in diameter was assembled in Gemini. A flow rate of 25sccm argon was introduced into the device and a 3.0A electron discharge from the cathode to the anode was used for device operation while measuring the voltage needed for ion saturation to occur.

To determine the ion saturation voltage, a negative bias relative to cathode was applied to an electrode plate located just downstream of the hidden anode device. By increasing the negative bias on the plate, ions accelerate towards the negative surface, while electrons eventually reach a retarding threshold near the surface and are repelled. When the positively charged ions bombard the plate, electrons from the power supply neutralize the ions, thus allowing current to flow from the ions to the electrode. This ion current was found by measuring the voltage across a shunt resistor, and was found to saturate at about -35V. This is shown in Figure 3.4.

After finding the voltage corresponding to ion saturation, the ion production was measured for various operating conditions. Figure 3.5 shows the linear relationship between discharge current and ion production current. It was found that higher discharge currents can be achieved by increasing the argon flow rate. The data labels shown in Figure 3.5 represent the maximum ion current before instabilities in the device were observed for each flow condition.

The ion production versus discharge power to the anode was another relationship that was explored, and is shown in Figure 3.6. Ion production is shown to increase with discharge power

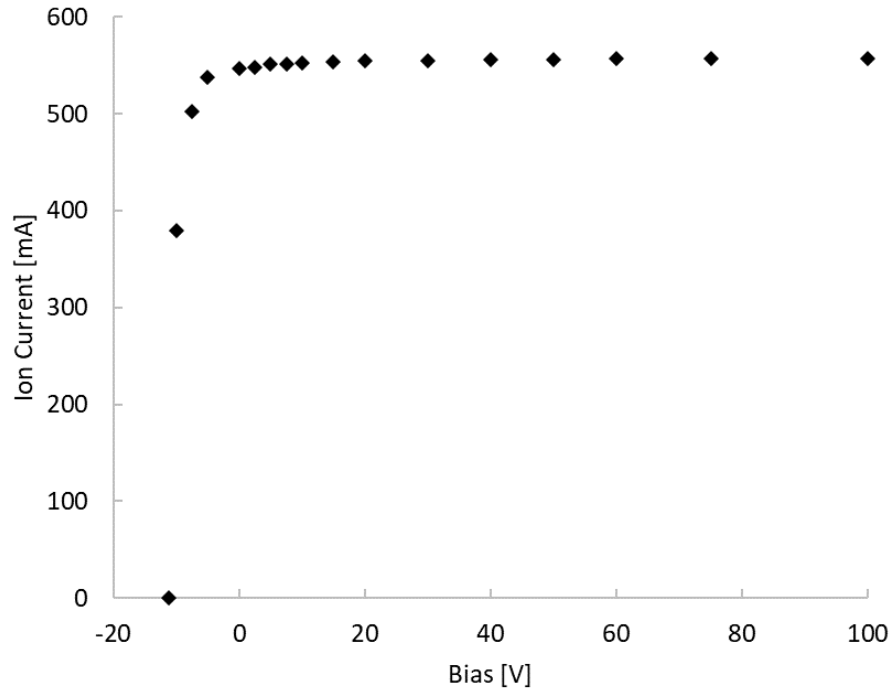


**Figure 3.4:** Hidden anode ion current saturation for ion production measurements.

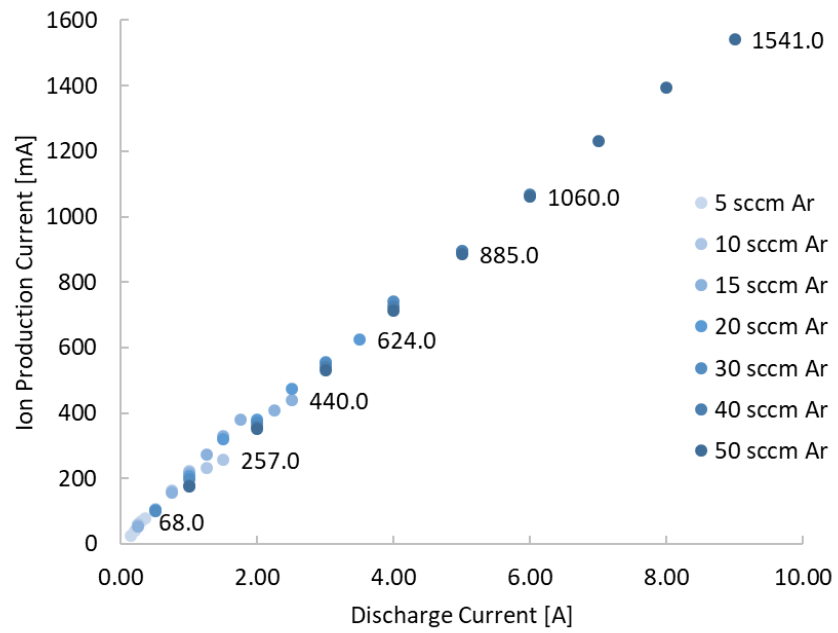


**Figure 3.5:** Ion production current as a function of anode discharge current and Ar flow rate.

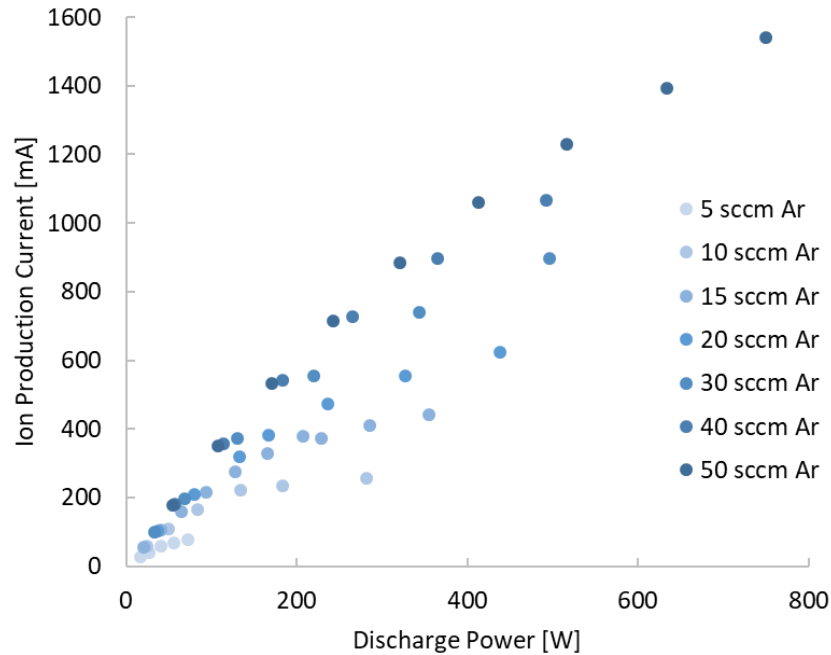


**Figure 3.6:** Hidden anode ion production as a function of discharge power for various argon flow rates.

to the anode. The anode discharge power is found by taking the product of the discharge voltage and current. The operation conditions for discharge voltage as a function of discharge current are shown in Figure 3.7. When considering the relationship between current and voltage we see a positive trend, which is expected when considering Ohm's law. The maximum discharge currents for each flow condition were found just before the device began decoupling and showed signs of unsteady operation. The maximum discharge current was shown to be controlled by the Ar flow rate. Since the ion production current is determined by the electron discharge current to the anode, the gas flow rate also determines the maximum limit of ion production. The data show that an increase in electron current increases ion production, suggesting that an increase in electron density flowing through the orifice to the anode causes enhanced ion production from an increase in collisional events. The energy of these ions can be controlled by throttling the mass flow rate of Ar introduced into the device, which is seen in the discharge voltage dependency on Ar flow rate.

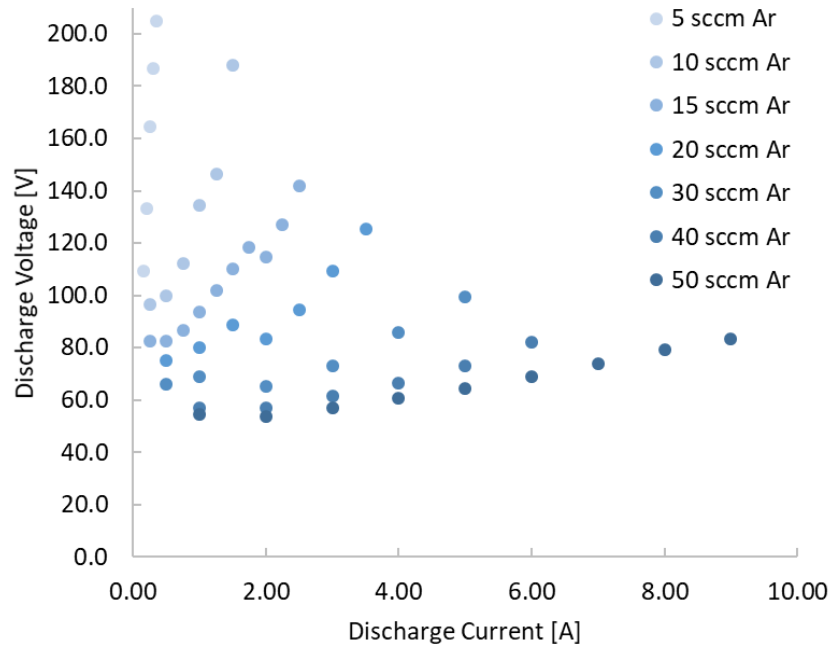


**Figure 3.7:** Hidden anode discharge voltage as a function of anode discharge current and Ar flow rate.

After recognizing the significant level of ion production capabilities of the device, as well as noticing the inside of the vacuum chamber to be notably shinier than prior to testing, it was time to test this newly characterized ion source as a sputter deposition tool.

### 3.3 Sputter Deposition Proof of Concept

Glass samples were loaded into vacuum facility 1 to test the coating operations with a titanium target plate. By applying a negative bias on a titanium electrode plate with respect to cathode, ions were accelerated with enough energy and momentum to sputter the material. This resulted in fully reflective titanium thin films after a half hour of deposition. A photo of the first deposition experiment is shown in Figure 3.8. The resultant thin films were adherent to the glass samples. By attempting to anodize the glass slides in a electrolytic solution at various voltages the adhesion was strong enough to stay on the glass without flaking off during the reactive process.

After physical confirmation that thin films could be deposited on to glass without flaking off, a number of experiments were conducted to study the operating conditions necessary for thin

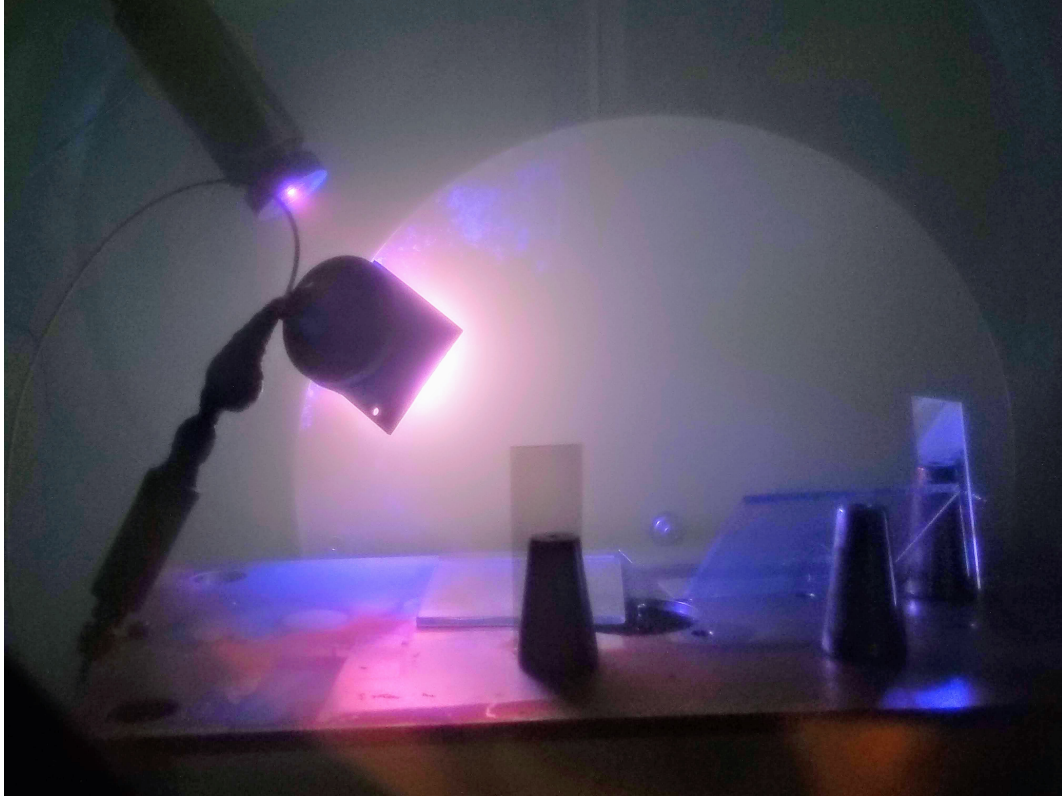


**Figure 3.8:** Photo of early sputter deposition testing with titanium electrode plate.

film growth. The following chapter provides the details regarding the components and electrical schematic of the deposition system.

## Chapter 4

### DEPOSITION SYSTEM COMPONENTS

The essential components needed for deposition to occur are an electron source, an ion source, and a metallic target. Figure 4.1 shows a photo of these components fully assembled on a mounting block used in the final design of the system. The motion stage shown in Figure 4.1 is used to move the target so that plasma cleaning and deposition can occur in a sequential manner. Each of the components shown in Figure 4.1 are described in the following sections.

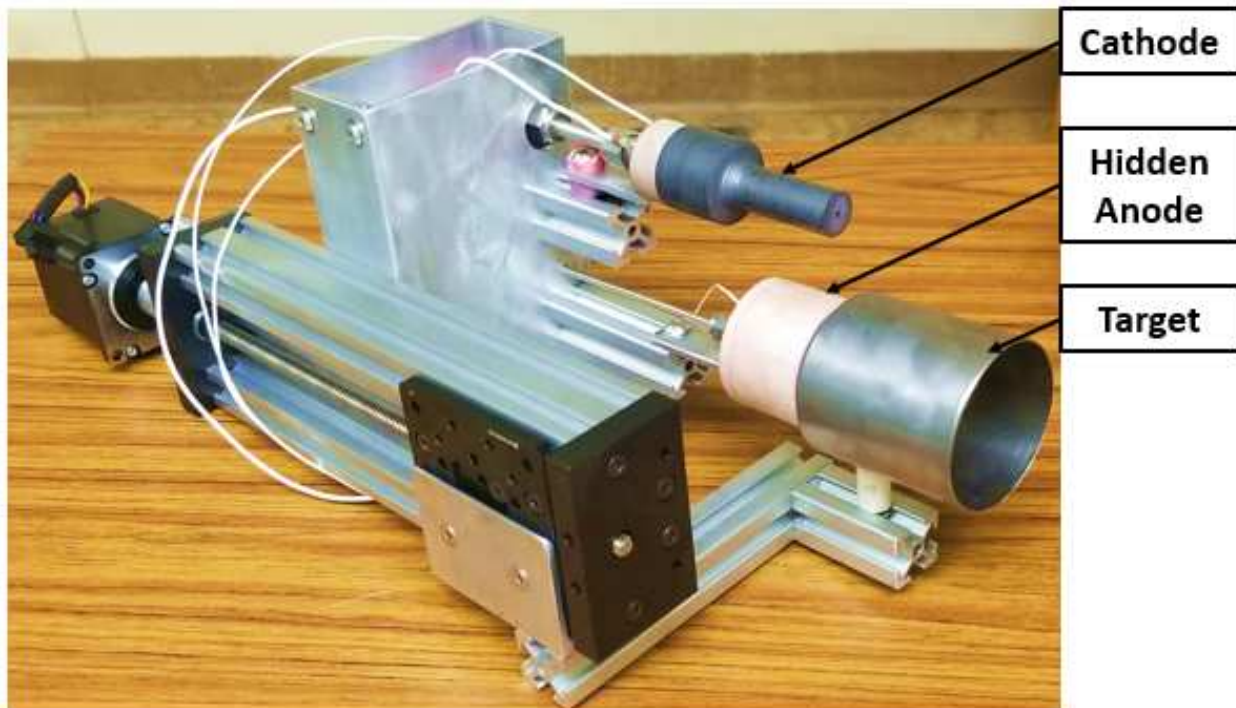


**Figure 4.1:** Photo of the deposition system components assembled on a mounting block.

#### 4.1 Hollow Cathode Electron Source

As mentioned previously, electrons need to be available for the hidden anode to produce ions. A thermionic hollow cathode is a device used to supply plasma electrons. This device is commonly

used in plasma processing applications and for electric propulsion applications, where ion beam neutralization or electron sources are needed [24,25]. They are useful for supplying electrons for a long period of time, unlike refractory wire filaments commonly found in ion beam discharge chambers, which eventually burn out and need to be replaced. A cross-sectional schematic of the hollow cathode used in the deposition system is shown in Figure 4.2. The cathode electrode consists of a

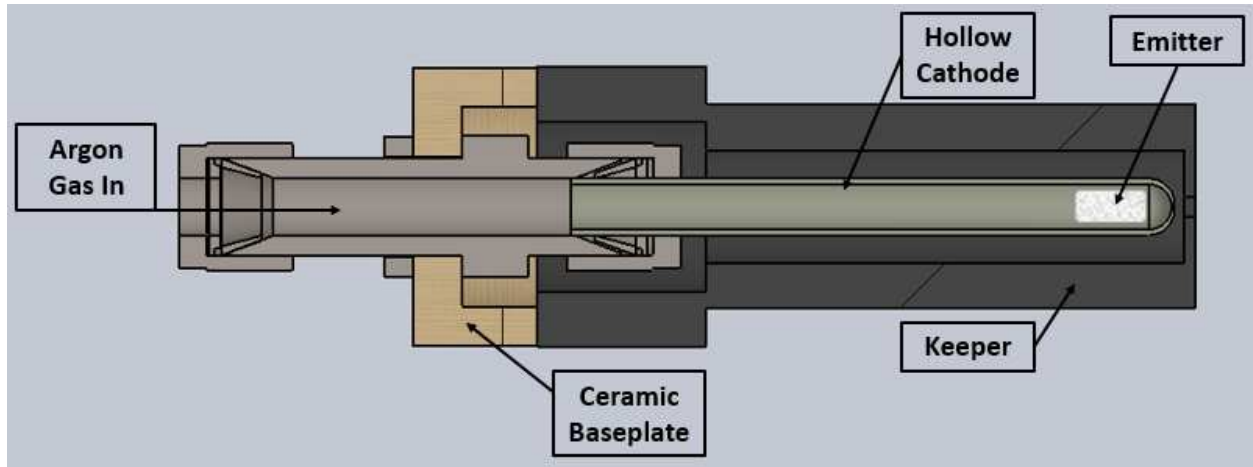


**Figure 4.2:** Cross-sectional schematic of cathode assembly.

tantalum tube that contains a porous tungsten barium calcium aluminate, low work function, emitter material. This low work function material allows electrons to be liberated from its surface and initiate an arc discharge. For an arc discharge to occur, a thermionic arc takes place within the device under argon gas flow when a positive bias is applied to the keeper electrode to drive electrons out of the cathode and into a discharge plasma. The keeper electrode was machined from graphite stock. The insulator baseplate is a machinable ceramic, alumina silicate, that provides isolation between the electrodes as well as a base to mount the device. The ceramic baseplate was cured using a process described in Appendix A. A photo shows the blown up view of the components used to make the device in Figure 4.3. A TDK Lambda GEN600-5.5 (600V 5.5A) is the power supply used to ignite and maintain the discharge during operation. The typical keeper voltage, relative to cathode, during operation is around 10-20V for a nominal 10sccm argon flow rate, and during anode discharge a keeper voltage increase will be observed by only a few volts.

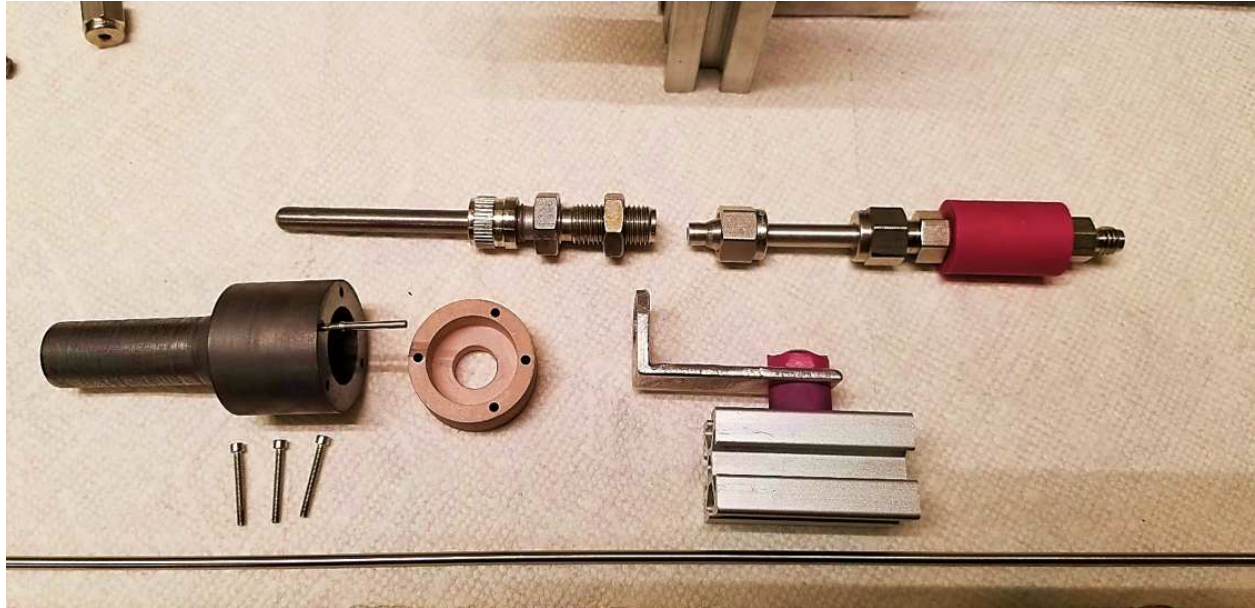


**Figure 4.3:** Photo of disassembled hollow cathode components.

## 4.2 Hidden Anode Ion Source

The hidden anode ion source (HAIS), as mentioned previously has gone through many iterations. It could be designed differently than presented here, and it is encouraged that those interested in the device experiment with new designs. The final iteration of the HAIS is an almost-monolithic, stout, cylindrical device. An alumina silicate body is used to house the hidden anode electrode, and it is capped with a graphite orifice plate. Figure 4.4 shows the cross-sectional schematic view of the design used throughout the development of the deposition system. A TDK Lambda GEN600-5.5 is used for the anode power supply.

A solution for overcoming difficult HAIS start up was found by coupling the orifice plate and the anode electrode to the cathode for initial startup. Once successfully coupled, as indicated by a steady anode voltage, the orifice bias is switched off, allowing for a stable discharge to the anode to occur through the orifice.

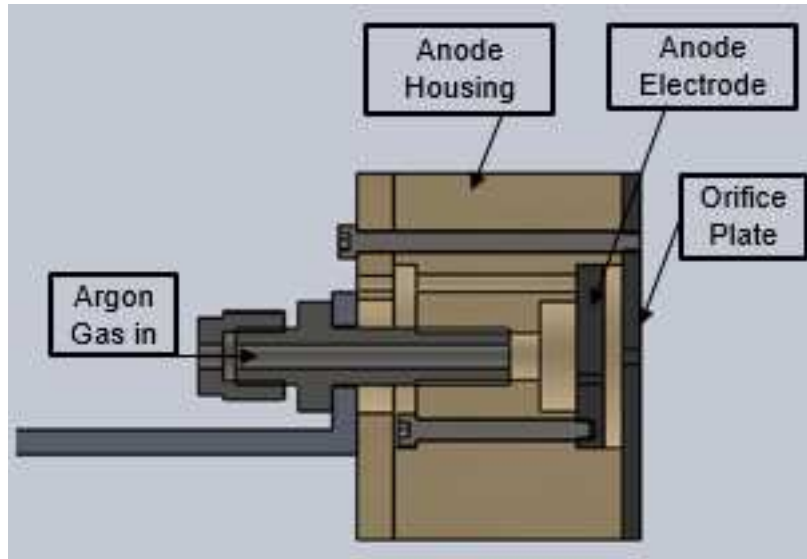


**Figure 4.4:** Cross-sectional schematic of hidden anode ion source.

### 4.3 Target Power Supply

A tubular metallic target is used in this deposition system. It allows for simplicity and less expenses associated with commercial deposition systems. No magnets, water cooling, or conductive backing plates are needed in this design. Several materials were experimented for target material such as copper, stainless steel, and titanium. Titanium was used for the deposition characterization to limit the number of variables introduced into the system. Copper was used to test operations with a lower temperature target material, and was found to operate similarly to a titanium target.

The power supply used for target biasing is the most complex and costly component in the system. An Advanced Energy Pinnacle Plus power supply is used because it allows for DC and pulsed-DC sputtering to occur, and is equipped with arc suppression circuitry to prevent arcing events, which help improve film quality. The arc quenching circuitry is capable of detecting arcs by metering the target voltage, and current. Once an arc is detected, positive biases are applied to the target to quench the arc. As discussed in Chapter 1, arcs from the target result in macroscopic particles, that can ruin thin film quality by leaving large material chunks on the substrate, which can result in pin holes or cause impurities in the film.

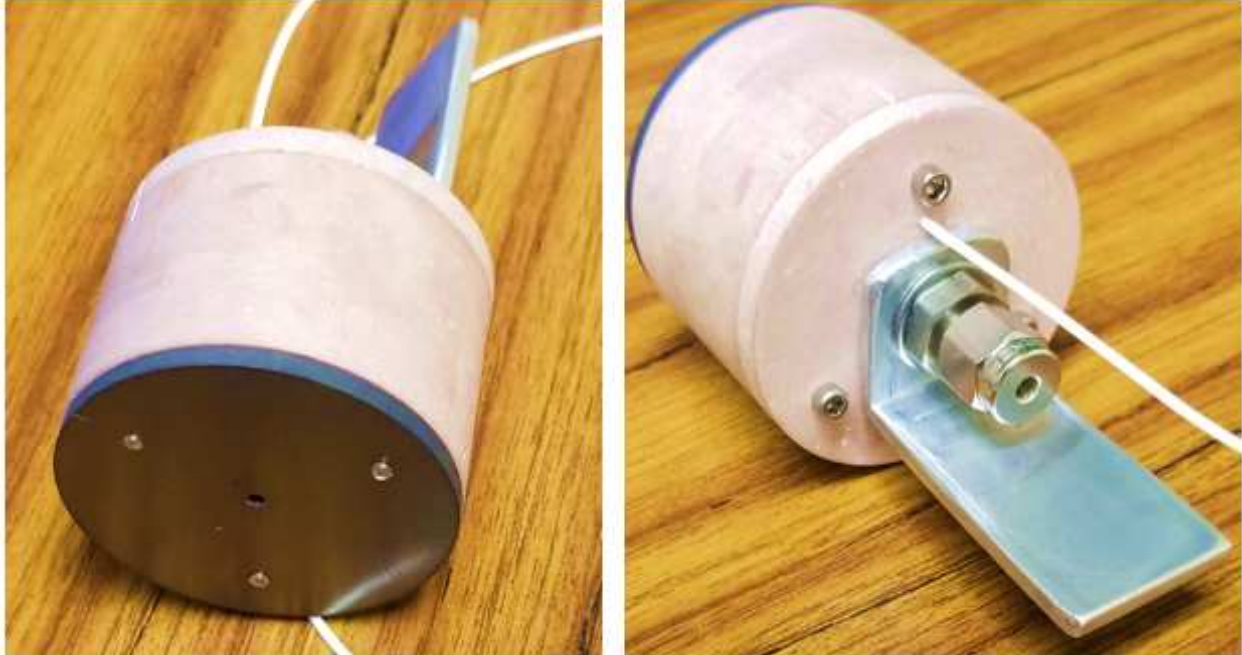


**Figure 4.5:** Photo of hidden anode fully assembled. Front view on left. Back view on right

During pulsed-DC operation, large current spikes caused problems with stepper motor motion control and false firing of limit switches due to electromagnetic interference (EMI). This issue was resolved by using current limiting resistors, which were applied to the cathode lead of the power supply since the potential here was only 10 - 20V above ground, instead of several hundred volts negative of ground on the target lead. An oscilloscope was used to measure the current spikes during pulsed-DC operation. The resistance was increased until the current spikes were reduced to have no affect on motion control. A 100 ohm resistor was found to reduce the spikes enough for the motion control system to properly function. It should be noted that this specific power supply unit is not required for the system to operate, and could be replaced with a less costly unit. For someone interested in a lower cost system, the necessary features would need to be decided based on the level of film quality required for the application.

The electrical schematic for the components described above is shown in Figure 4.6, and illustrates how the circuits are completed through plasma coupling. The cathode-keeper power supply pulls current through the plasma between cathode and keeper electrodes by utilizing mobile electrons, and in the same manner, the cathode-anode power supply does so as well. For DC operation,

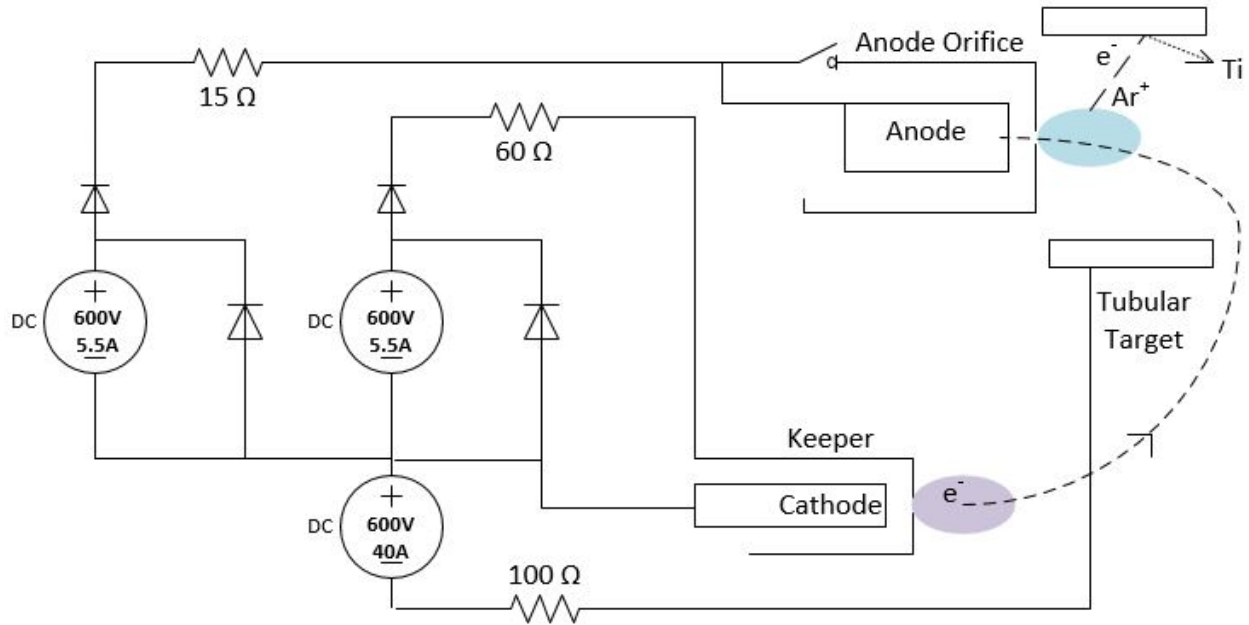


**Figure 4.6:** Electrical schematic of the plasma circuit during deposition.

the target supply is negative of cathode potential and the circuit is closed by the positively charged ions flowing to the surface of the target interface, which are neutralized by electrons supplied by the target power supply. For pulsed-DC operation, the circuit is completed in the same manner as in DC sputtering. For positive biases in between sputtering, electrons are collected on the surface. While all of the structural components of the system are tied to ground (chamber potential), all of the associated plasma electrodes are floating with respect to ground. This ensures that grounded components cannot electrically participate during operation, which would likely result in current leakage.

# Chapter 5

## DEPOSITION SYSTEM DEVELOPMENT

The system components described in Chapter 4 underwent several design changes during the development of this system. The experiments described in this chapter led to a cost effective system useful for coating glass substrates with a maximum area of approximately 0.5m x 1.0m.

### 5.1 Thin Film Profile Measurements

Thin film thickness profiles were measured for various tubular target lengths and target-substrate distances, or throw distances. A photo of the experimental setup is shown in Figure 5.1. Thickness measurements were made by masking sections of the substrates with Kapton tape, and then depositing the films. The resultant thickness profiles were measured using a Tencor Alpha-Step profilometer. Figure 5.2 shows a thickness profile for a Ti and TiO<sub>2</sub> coating. The film profiles were shown to decrease in thickness laterally from the target axis, resembling Gaussian profiles.

Tests were conducted to measure deposition conditions for various target throw distances and lengths. Average deposition rates and coverage areas varied for these different design parameters, and are shown in Table 5.1. The length of the target was found to be optimal at 10cm to 15cm in length. This length provided the best coverage and deposition rates for all throw distances compared to longer target lengths. These tests were completed over 35 minute deposition periods at a throw distance of 3cm. Deposition conditions included a 3.0A anode discharge current with a 40sccm argon anode flow, and a -500VDC target bias. After measuring the resulting film thick-

**Table 5.1:** Deposition results for various target lengths.

Target Length [cm]	Avg. Thickness [nm]	Avg. Deposition Rate [nm/min]
20	331	9.5
15	786	22.5
10	540	15.4

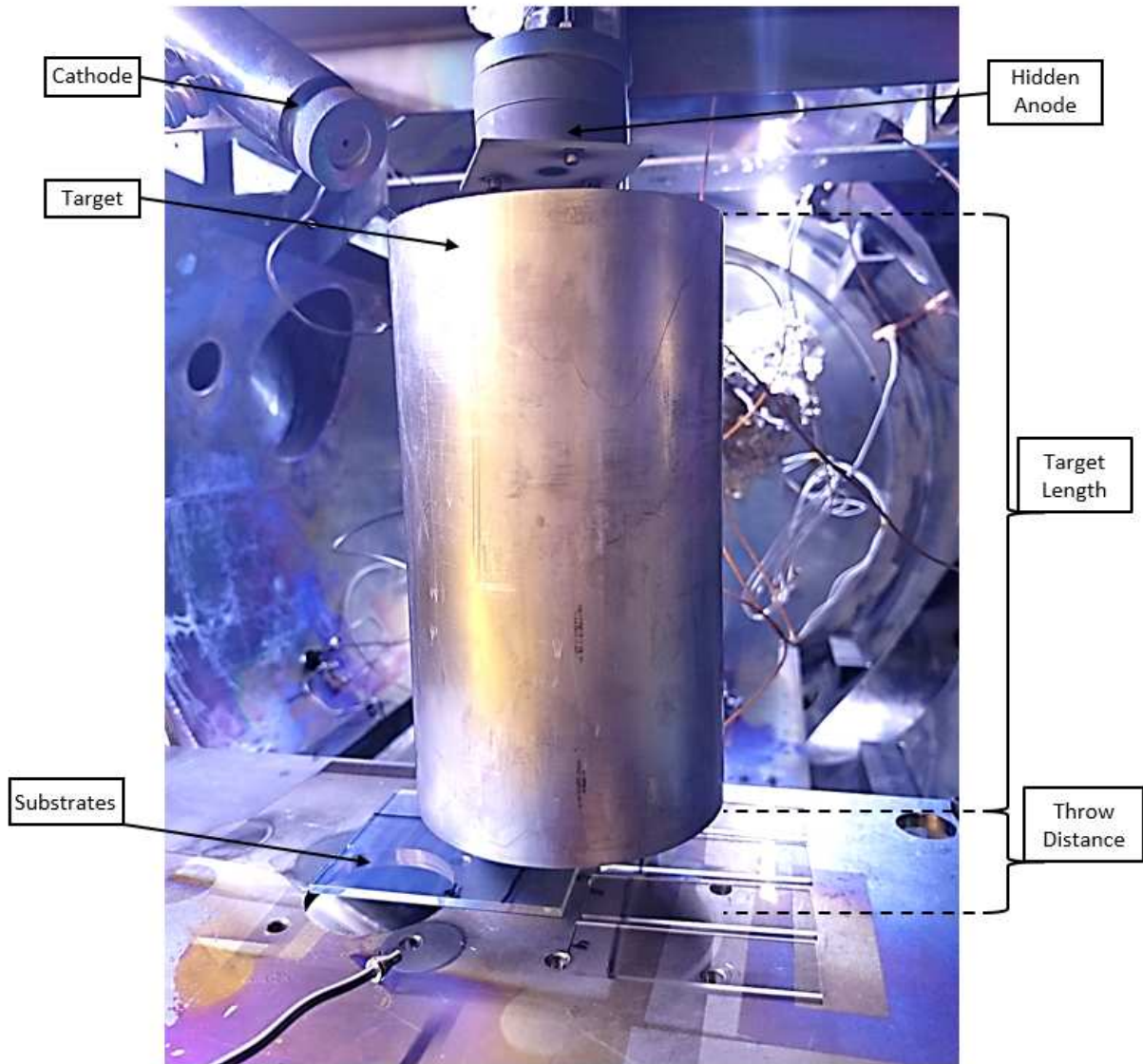


**Figure 5.1:** Photo of experimental setup for stationary thin film thickness profile experiments using a tubular target for deposition.

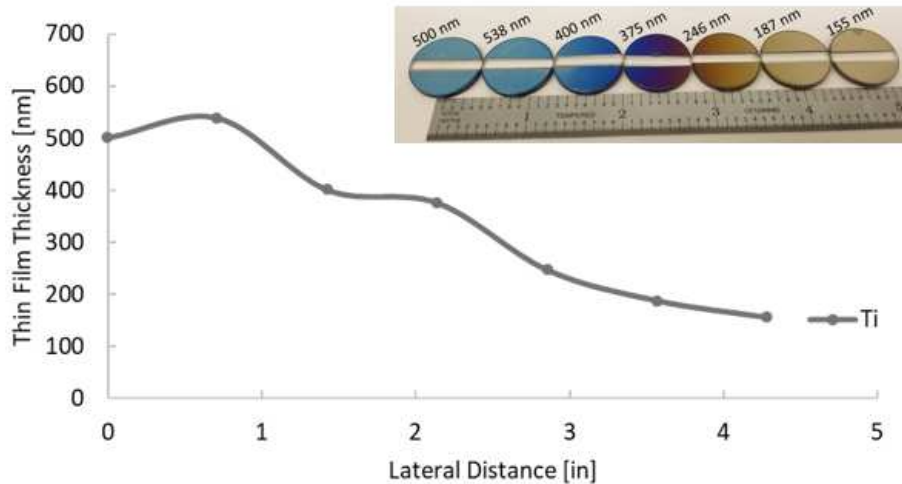


**Figure 5.2:** Thickness profile for Ti and TiO<sub>2</sub> coating on glass substrates.

nesses downstream of the deposition source for the stationary tests, motion tests were conducted and compared to a model for estimating the thickness uniformity of the films for the system in motion.

## 5.2 Motion Testing for Thin Film Uniformity

Once the optimal target length was found, experiments were conducted to test the level of thickness uniformity. The operation procedure of these tests involved a two-axis motion stage that moved the substrate horizontally at a prescribed speed, downstream of the deposition source, until reaching some distance outside of the deposition trajectory zone. At this point, the substrate was displaced vertically by a prescribed distance, and then horizontally scanned in the opposite direction. This process was repeated over the entire area of the substrate. Figure 5.6 shows a photo of the system during deposition testing.

The distances between horizontal scans allows for thickness uniformity control. For smaller distances between scans, the thickness uniformity will be improved. The variation in thickness due to the motion can be modeled by using the measured stationary deposition profiles, moving them spatially, and then summing these displaced profiles. Figure 5.6b shows an example of a

thickness profile (black) and the profile summed over incremental distances (red) to show thickness uniformity for a 6cm incremental distance between scans.

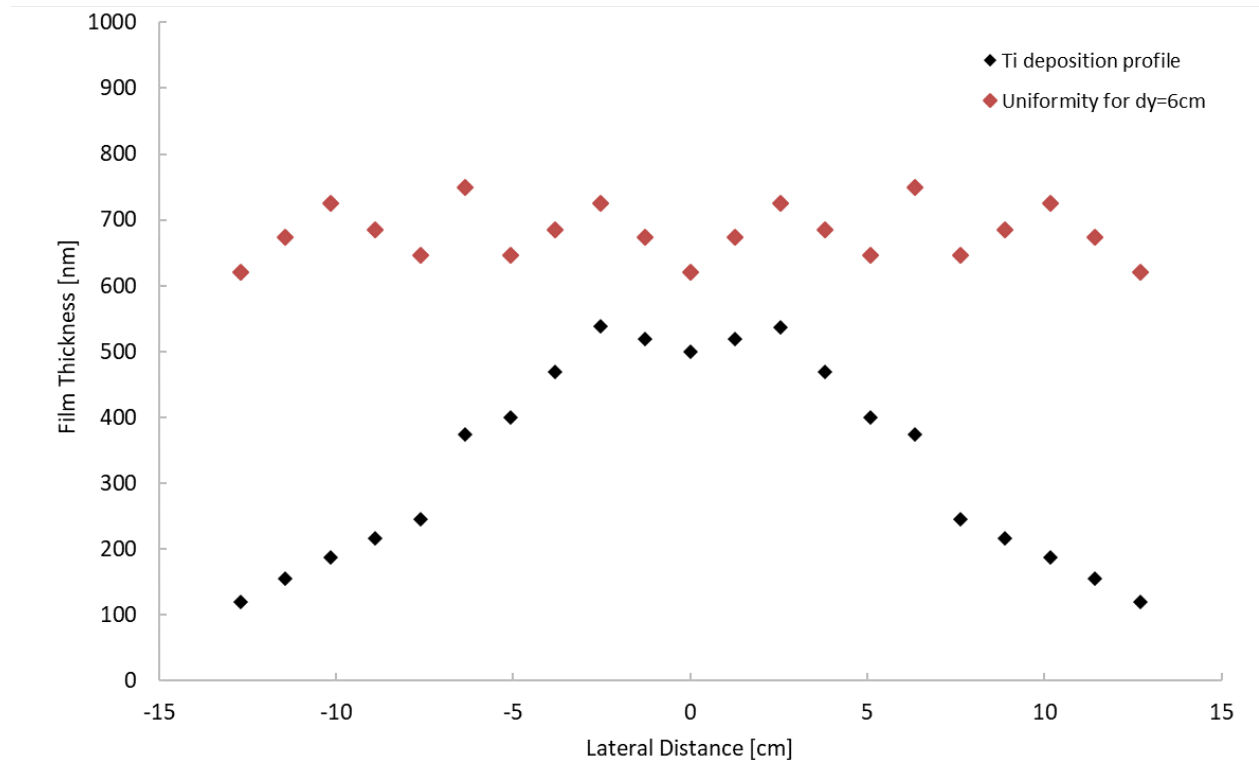


**Figure 5.3:** Measured thickness profile (black) and summed profiles for modelled thickness uniformity for 6cm incremental distances between scans (red).

This model provided the starting point for running the motion experiments. It provided information for required motion control, estimated time required for coating, as well as the level of thickness uniformity for incremental distances between scans. Thickness measurements were made at several locations over the area of the substrate to estimate uniformity of the deposition process. A measured thickness profile for 6cm distances between scans is shown in Figure 5.4. Figure 5.4 shows the measured thickness to vary less than 6% of the overall thickness. The uniformity was found to be sufficient for a visual art application.

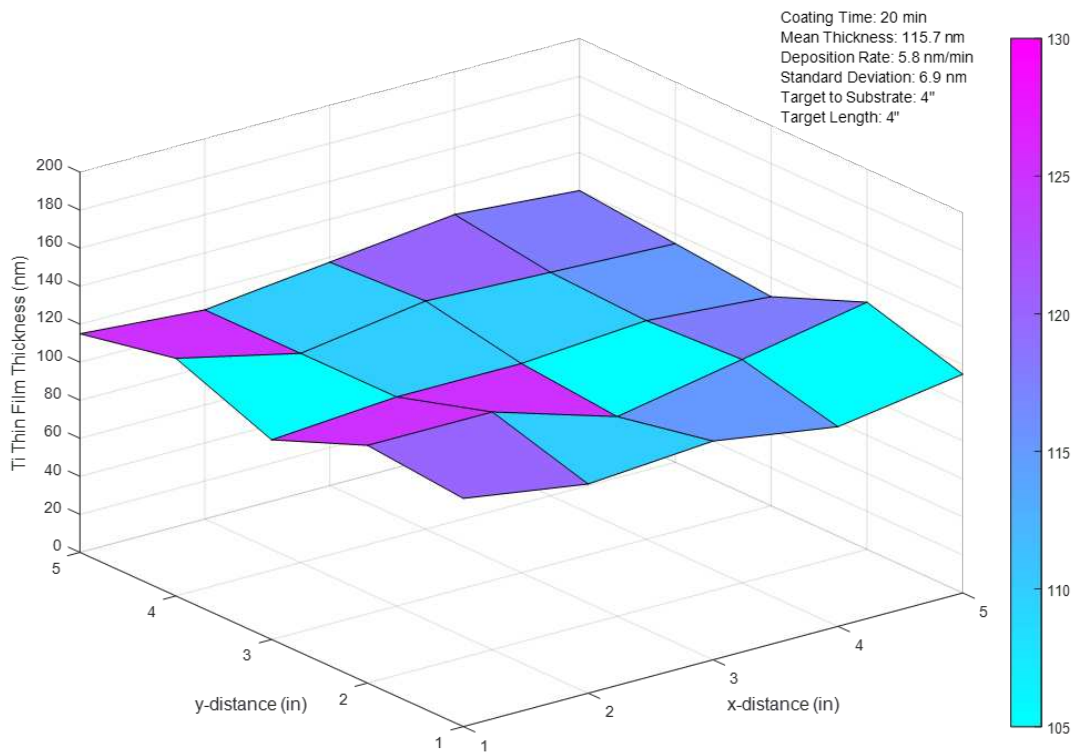


**Figure 5.4:** Thin film surface generated from measured thickness over substrate area post deposition.

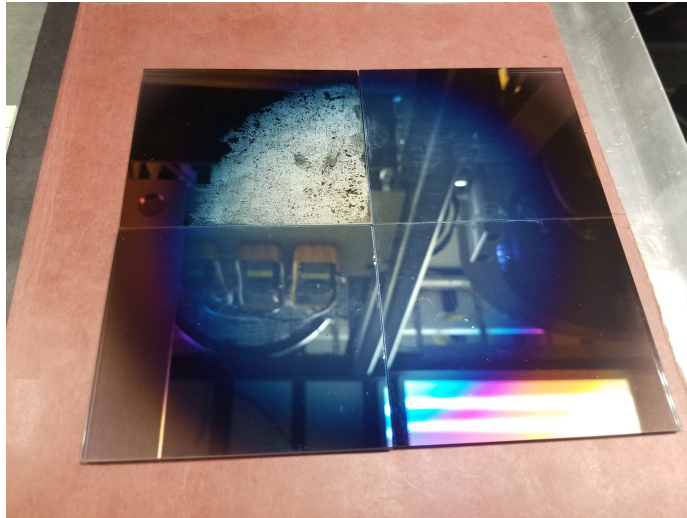
### 5.3 Ion Cleaning

As mentioned in Chapter 1, even after cleaning a substrate surface in atmospheric conditions, the surface is coated in a layer of contaminants so quickly it is immediately dirtied. Therefore, to achieve ultimate surface cleanliness, cleaning procedures need to be conducted under low pressures to reduce the time it takes for a monolayer of contaminants to form on the substrate surface [11]. High energy ions are found to be an effective method for cleaning in vacuo, which is performed prior to deposition with the HAIS. By removing contaminants on the surface, such as hydrocarbons, thin film adhesion is improved. Adhesion is believed to be enhanced through the use of ion bombardment of oxygen and argon ions prior to deposition. By means of ion bombardment, the substrate surface is not only ion etched, but also heated to temperatures higher than 50° C. Most hydrocarbons are expected to be removed from the substrate surface at these elevated temperatures under vacuum pressures [26].

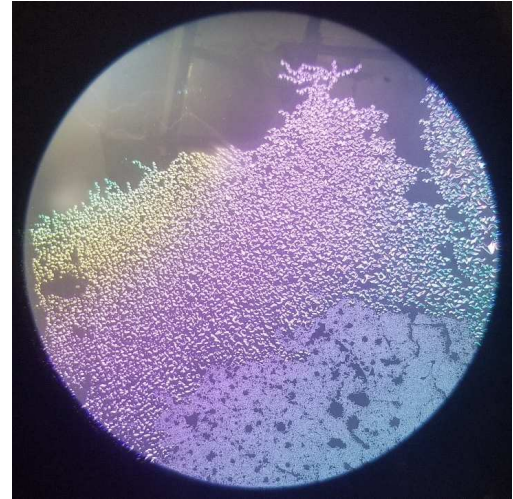
To show the importance of substrate cleanliness, an example of a deposited film on an uncleaned glass surface is presented in Figure 5.5a, where four samples were coated in Ti and then TiO<sub>2</sub>. The thin film was not able to adhere to the uncleaned substrate surface and resulted in an unstable coating. The damaged film is magnified in Figure 5.5b.

To reach ultimate substrate cleanliness, ion bombardment is used as a method of cleaning. Figure 4.1 shows a linear motion stage connected to the tubular target, which allows for the target to move between two positions. When the target is positioned behind the hidden anode, or out of site from the ions, it is in the cleaning position. When the target is positioned in-front of the hidden anode, as shown in Figure 4.1, it is in the coating position. Photos of the system undergoing the two procedures is shown in Figure 5.6.

An additional shutter component was added to the system after observing pin holes in the thin films. By blocking the substrate's line of sight from the plasma sources during the start up procedure, the substrate is shielded from any cathodic arcing that may occur. Once the system is steadily operating, the shutter is opened, allowing the substrate to be exposed to the ions and target vapor particles.

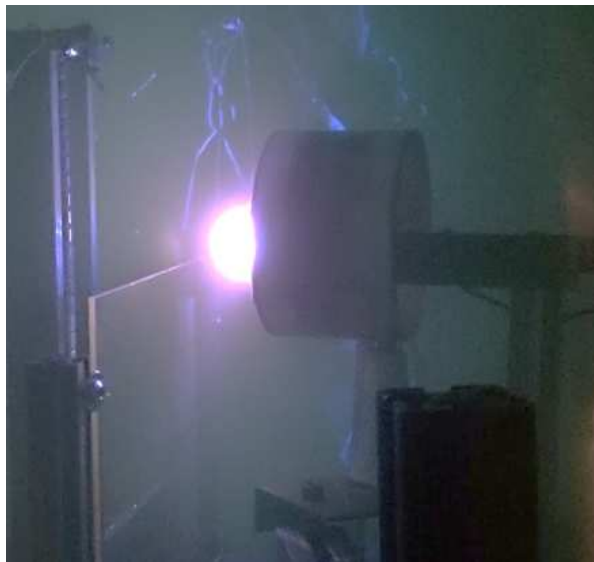


(a)



(b)

**Figure 5.5:** Photo of deposition results substrate cleanliness testing. (a) Shows unstable thin film on top left uncleaned sample. (b) Magnified close up of the unstable film on the sample.



(a)



(b)

**Figure 5.6:** Photo of deposition during motion testing. (a) Shows the system during the cleaning process, and (b) shows the system during the coating process.

## 5.4 Motion Control

A motion controller was built using stepper motor drivers and Arduino microcontrollers to control the motion described previously. Two Arduinos were used; one for controlling the target and shutter positioning, and a second for controlling the horizontal and vertical motions during cleaning and coating operations.

A sample program for deposition is presented in Appendix B. This program is used to control the motion of the system, which along with deposition parameters, controls how the thin films are deposited during deposition. By experimenting with different motions, films can be placed in desired areas with control, or improvisationally depending on how the motion is carried out and the deposition settings are varied.

## 5.5 System Assembly

After demonstrating how incremental distances between scans influences uniformity and thickness, as well as using ion cleaning and a shutter to improve thin film quality and adhesion, a two axis motion system was assembled from a kit supplied by Openbuilds. A photo of the final motion system assembly is shown in Figure 5.7. The motion stages translate the deposition system through the use of a lead screw and carriage. The aluminum extrusion and carriage mounting points allow for the system components to be easily fixed and adjusted.

## 5.6 Gas Feed System

A low cost and simple gas feed system was created for the plasma components. By eliminating the use of a mass flow controller (MFC) and gas flow controller (GFC), savings on cost and complexity are made. This was done by using manual shutoff valves and flow restrictors. To test the capabilities of this sort of gas feed system, several needle valves and flow restrictors were studied to find the necessary flow rates that an MFC and GFC can provide for the HAIS and cathode.

Argon flow rates were found for various needle valve settings. The values were found by correlating Ar partial pressures at known flow rates, and the chamber pressure, with flow rates

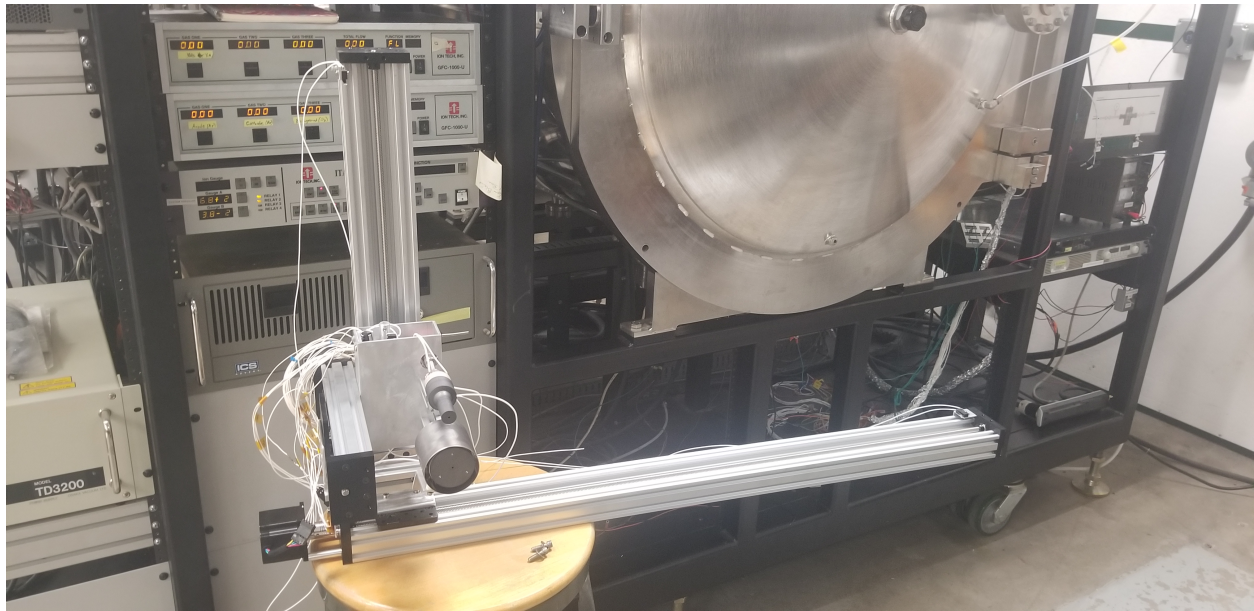


**Figure 5.7:** Photo of deposition system assembled on a two axis motion system.

provided by different needle valve settings. An RGA was used to measure partial pressures in the chamber for the MFC and needle valve. These flows are tabulated in Appendix C for various upstream pressures.

The flows given by the needle valve were adequate for HAIS Ar flow rates. The needle valves tested were not able to provide the lower flow rates needed for the cathode, therefore a porous flow restrictor, purchased from Mott corp, was used to obtain the desired flow of 10scm argon at a 40psi upstream pressure. This flow restrictor is designed for long lifetime usage because of the low probability of clogage, therefore adding reliability to the deposition system. The long lifetime associated with the hollow cathode device allows for the possibility of large and complex thin films to be accomplished.

One issue faced with the heaterless hollow cathode used in the system is the start up procedure. There are current research efforts regarding this topic which will not be described here. Instead, a solution for successful start up is presented. To ignite an arc discharge in the cathode, sufficient Ar flow rates are needed for a duration of time while the keeper-cathode bias is applied. This can be done by charging a fixed volume in the gas feed line between the flow restrictor and the shutoff valve [27,28]. Figure 5.8 shows a schematic of the gas feed system.

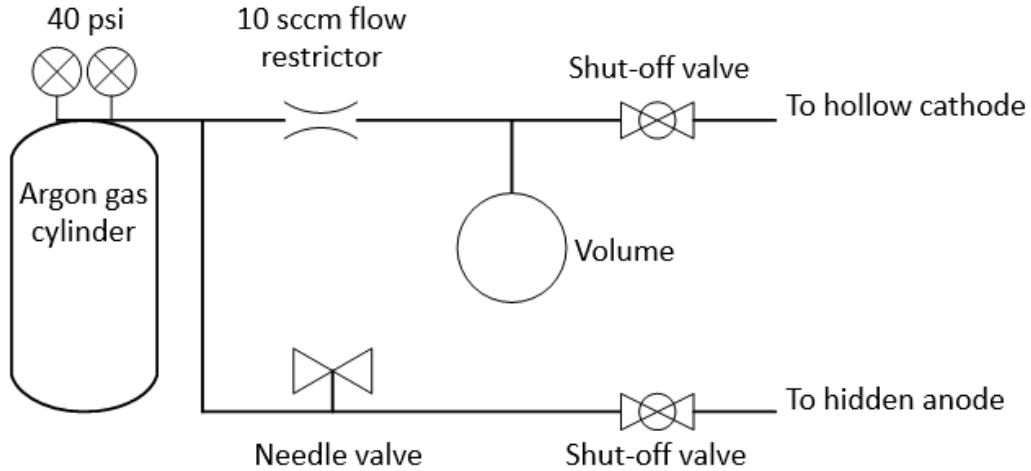


**Figure 5.8:** Gas feed system schematic for cathode and hidden anode plasma devices.

Once the volume in the cathode feed line is charged, and a large voltage (600VDC) is applied to the keeper with respect to the cathode, the quarter turn valve can be opened to start the plasma discharge. After this, the anode feed line can be opened and the HAIS can be started by coupling the electron discharge to the anode orifice disk and then to the hidden anode only (shown in Figure 4.6). For simplicity, a pressure of 40 psi is used for regulating both the hidden anode and the cathode flow rates.

A bill of materials is presented in Appendix D, which lists all the materials associated with the components discussed in this chapter. A thorough cost analysis among commercial deposition systems is not necessary for seeing the cost savings this system provides. It should be noted that commercial systems have undergone intensive studies and iterations to be able to produce high quality films, so for certain applications it is obvious to use a more understood deposition system. This thesis is not to convince one to use the deposition system discussed here instead of others, it is here to show another way of growing thin films in a cost effective manner that is shown to work well for applications that desired durable, dense, and adherent films with uniformity control over reasonable coating times. If other properties are desired, then more research and development would need to be conducted. In the following chapter the system is characterized for typical operation conditions that have been found to work in the development stages of this project.

# Chapter 6

## DEPOSITION SYSTEM CHARACTERIZATION

Plasma properties and deposition rates are useful for describing the deposition environment and the effectiveness of the deposition system compared to other systems. The plasma properties near the substrate surface and the hidden anode device could be used to determine the effectiveness of the cleaning and deposition processes. The measured deposition rates and plasma properties could also be used to create a model for determining what operating conditions could be used to produce a thin film with desired properties.

### 6.1 Plasma Properties

Several diagnostic techniques were used to measure the plasma properties of the system. These properties of interest include electron temperature, ion current density, and plasma density at various operating conditions at the far field (substrate locations) and near field (inside the target). By measuring the electron temperature the density of electrons and ions can be approximated [12].<sup>1</sup> A triple probe was used to measure the electron temperature and plasma density at the substrate locations in the far field.

A triple probe is a plasma diagnostic tool that allows for the measurement of plasma properties at high spatial and time resolutions. A schematic of the probe circuit is show in Figure 6.1. Due to the elimination of voltage sweeps or voltage pulsing per spacial location of interest, as in the case with single probe measurements, there is very little data processing involved in the triple probe method compared to single probe, or double probe methods [12]. By using the methods described in [12], the triple probe allows for the properties to be found by recording only two parameters; the voltage across probes 1 and 2, and the net current from probe 1 to probe 3. Since probing is an intrusive measurement technique, a couple of requirements are needed for valid data

---

<sup>1</sup>This is accomplished by using sheath approximations discussed in S. Chen et al [12].

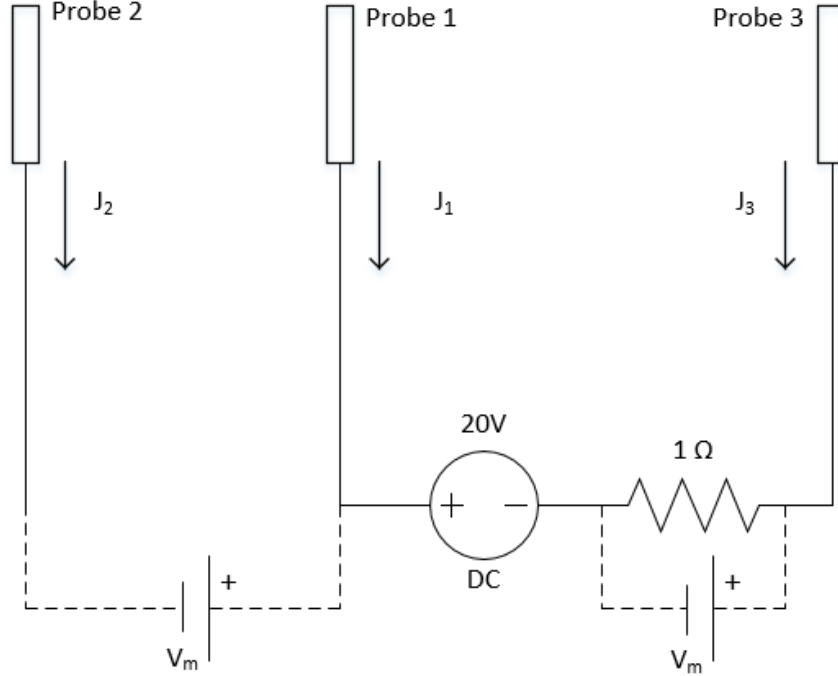


**Figure 6.1:** Triple probe electrical schematic.

collection. First, a Maxwellian energy distribution is assumed for describing the electrons in the plasma. Second, for negligible probe interactions with the plasma, the ion sheath thickness should be smaller than the probe separation distances, and the probe radius and the thickness of the ion sheath should be smaller than the mean free path. With these conditions met, the probe currents can be measured and expressed in terms of the electron and ion currents. Equation (6.1) is used to calculate the approximate electron temperature [12, 29].<sup>2</sup>

$$kT_e = \frac{V_{12}}{\ln(2)} \approx \frac{V_+ - V_f}{0.7}, \quad (6.1)$$

Where  $k$  is the Boltzmann constant,  $T_e$  is the electron temperature, and  $V_{12}$  is the voltage measured across probes 1 and 2. After finding the approximate electron temperature, and measuring the electron current, the electron density can be found using equation (6.2). An assumption is made for the area of the sheath to be equal to the surface area of the probe.

---

<sup>2</sup>For a more detailed explanation of the theory related to the triple probe diagnostic technique see references [12, 29].

$$n_e = \frac{J_{13}}{A_p e \sqrt{\frac{kT_e}{m_i}} \exp\left(\frac{-1}{2}\right)}, \quad (6.2)$$

Where  $J_{13}$  is the current, calculated by using the measured voltage across the shunt resistor and applying Ohm's Law,  $A_p$  is the area of the probe,  $e$  is the charge of an electron, and  $m_i$  is the mass of an Ar ion. The measured probe diameters and length were 0.016" and 0.21", respectively, with a probe separation distance of 0.050". The electron saturation current was found by increasing the bias between the probes. This voltage was found to be around 20VDC, which is sufficiently larger than  $kTe$  to ensure electron saturation [12, 29].

It is of interest to consider how the plasma interacts with the substrate surface downstream of the deposition system. Specifically considering the ion cleaning and thin film assist processes, it is useful to know the plasma density at the substrate location. Electron density can be approximated after finding the electron temperature. At a distance of 20cm from the target, a typical location for the substrate, the far field electron temperature for various target potentials and anode currents is shown in Figure 6.2. The electron temperature is shown to reach a maximum value of 5.2eV for

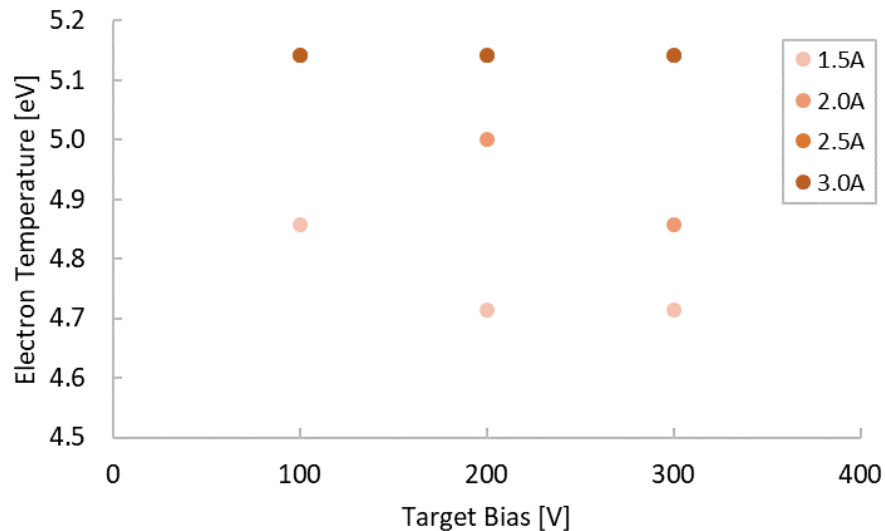


**Figure 6.2:** Electron temperature versus target bias for various anode discharge currents.

anode discharges above 2.5A at all target biases considered. For increasing target voltage at anode

currents lower than 2.5A, the electron temperature is shown to decrease. Considering equation (6.1), this trend is likely due to the increase in plasma density within the target. The electron density is shown in Figure 6.3. Linear behavior is observed for electron density for increased

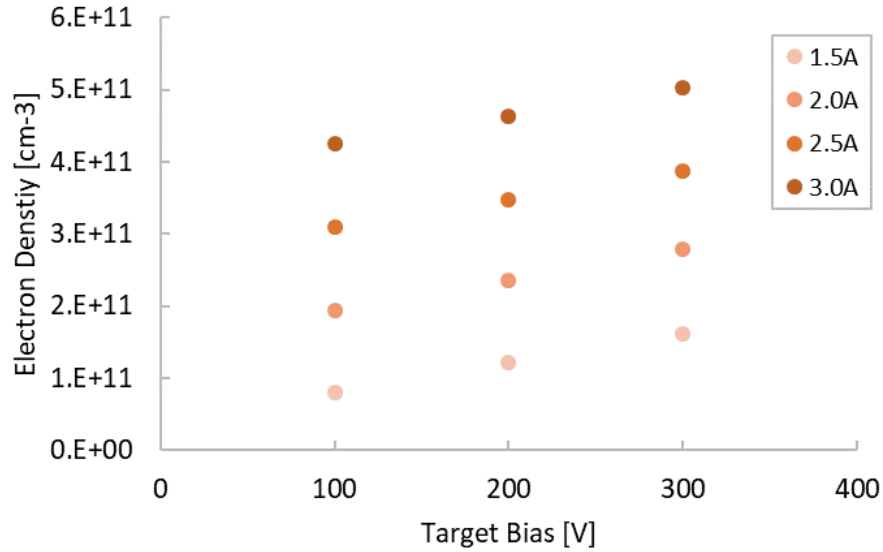


**Figure 6.3:** Electron density versus target bias for various anode discharge currents.

anode current and target bias. This is likely due to the increase in discharge current to the anode, as shown in Chapter 3, ion production increases with discharge current. It is expected that an increase in ion production rate will result in an increase in plasma density due to the plasma's ability in maintaining electrostatic equilibrium [14].

From the electron temperature gathered for typical operating conditions, the plasma potential was also found for these conditions. Equation (6.3) was used to find the plasma potential,  $V_p$  [30].

$$V_p = V_f + \left| \frac{kT_e}{e} \ln \left[ \left( \frac{2\pi m_e}{m_i} \right)^{1/2} \exp(-1/2) \right] \right|, \quad (6.3)$$

Where  $V_f$  is the floating potential and  $m_e$  is the mass of an electron. The plasma potential was found to be around 40V for all conditions in this far field location. This is helpful for evaluating the effectiveness of the ion cleaning process. Since the substrate is not grounded, it floats slightly

negative due to the electrons' high mobility discussed previously. Ions produced by the HAIS are believed to be born at a range of energies, and some of the ions will fall through this potential. Ions with enough energy and momentum will likely clean the surface.

After finding the plasma properties near the substrate surface, it is also of interest to consider the plasma near the hidden anode orifice and inside the tubular target. Using the data found in the far field, such as electron temperature and density, the ion density was approximated using these values for the near field using a Faraday probe.

## 6.2 Ion Density Along Target Length

A Faraday probe of known surface area was used to measure the ion current density along the length of the target surface. The ion current density and electron temperature data was then used to approximate the ion density along the target length.<sup>3</sup> The Ti target was fixed in the coating position, and slotted to allow the probe to traverse the length of the target using the target cleaning/coating motion stage. Figure 6.4 shows the experimental setup for collecting ion current. Similarly to ion production measurements discussed in Chapter 3, the bias necessary for ion saturation needed to be found using the Faraday probe. This occurred at -30V and was used for the following data collection.

The ion current was recorded along the length of the target, where the probe collector surface was approximately flush with the inner surface of the target. The current density was found by dividing the ion current by the collector area. Using the current densities found with the Faraday probe, and the electron temperatures from Triple probe experiments in the far field, the ion density was calculated along the length of the target surface. The equation used to calculate the approximate ion density is shown in equation (6.4). The equation is derived from the Bohm velocity [31].

---

<sup>3</sup>The Faraday probe used for ion current measurements was supplied by Plasma Controls LLC. The probe includes an isolated guard ring. This ring is held at the same potential as the collector to ensure a uniformly distributed, perpendicular electric field at the ion collector surface. For more information regarding Faraday probe theory see reference [31].

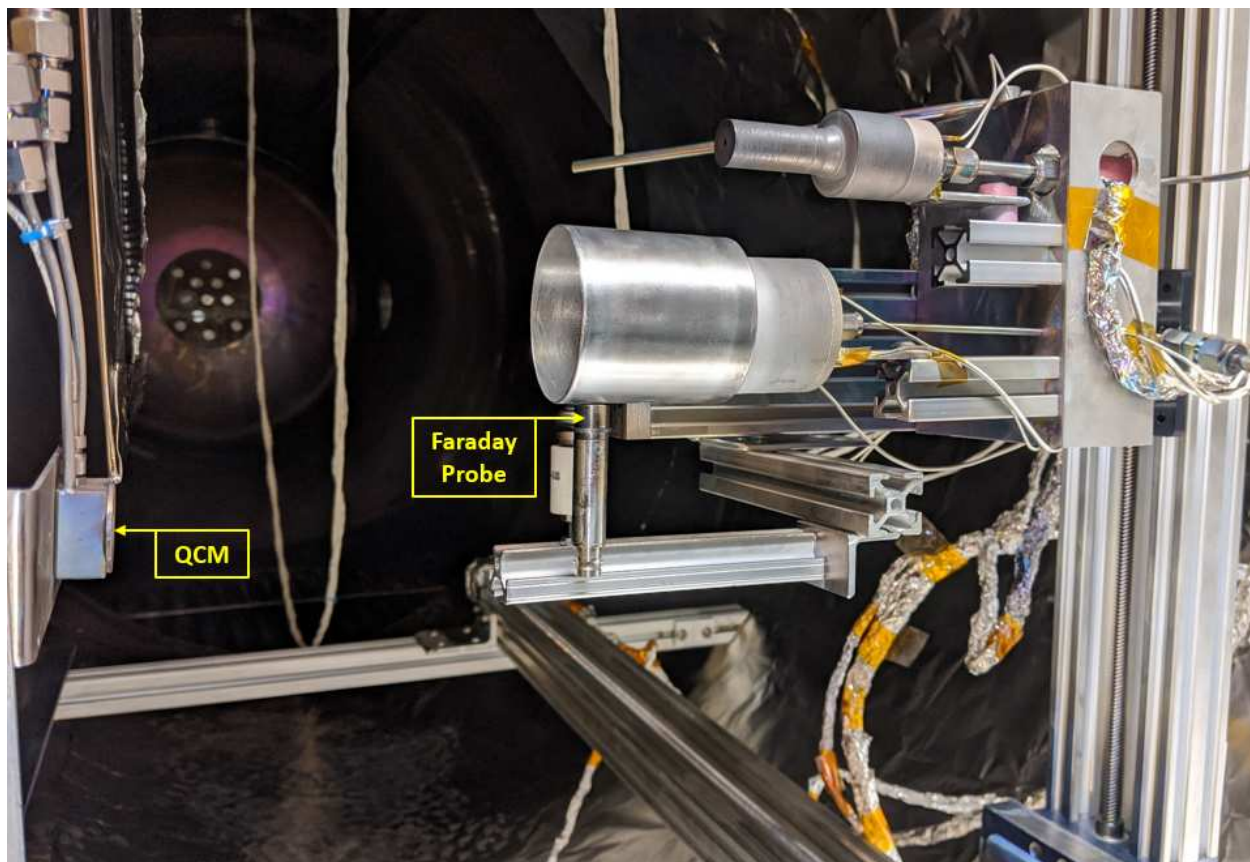


**Figure 6.4:** Photo of experimental setup for Faraday probe measurements.

$$n_i = \frac{J_i}{e\sqrt{\frac{kT_e}{m_i}} \exp(-\frac{1}{2})}, \quad (6.4)$$

Where  $n_i$  is the ion density,  $J_i$  is the ion current, and  $m_i$  is the ion mass. Since 2.0A to 3.0A anode discharges are found to be adequate for most deposition procedures, an electron temperature of 4.7eV to 5.1eV can be used to approximate the ion density along the target length for the target biases considered. This range of electron temperatures found in Figure 6.2 provides approximate values that could be used for studying the deposition process more in depth.

The ion current was measured along the length of the target with and without applied target voltages to compare the ion density for each condition. As shown in Figure 6.5, the ion density is

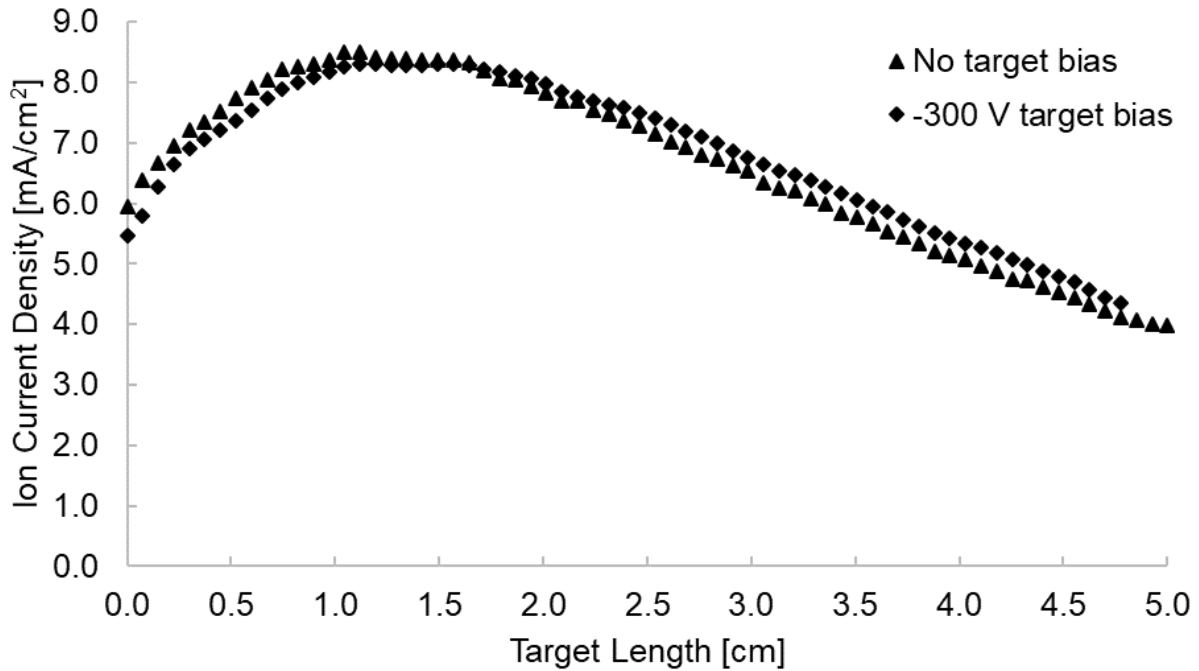
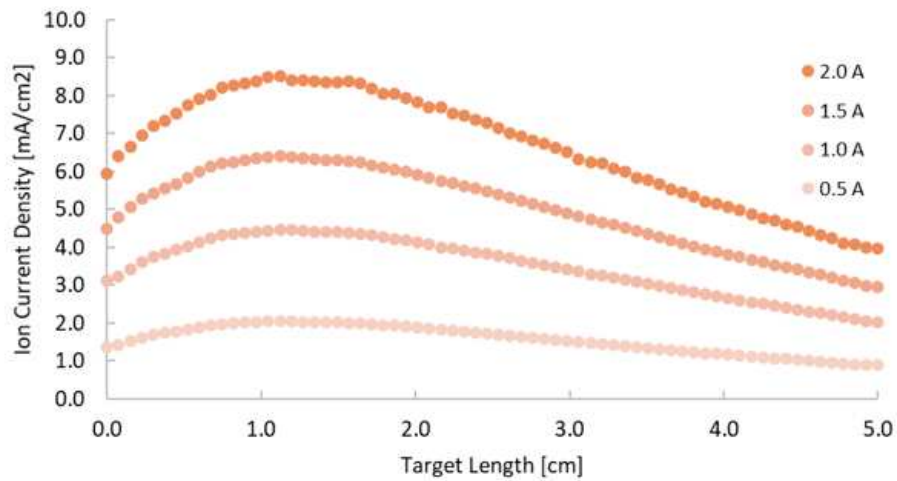


**Figure 6.5:** Ion current density with and with out biased target over length of target.

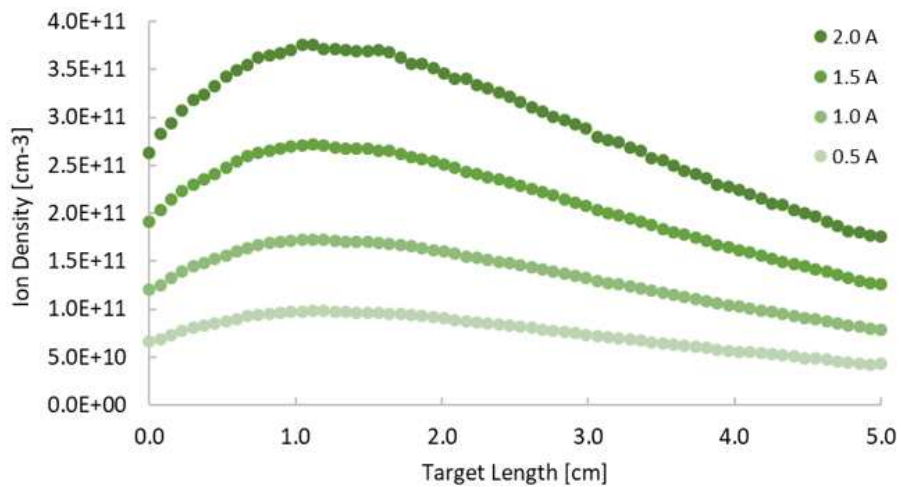
not influenced by biasing the target. Due to the ability of the plasma to shielding electric fields, a target bias is not expected to influence the number of ions present at a given location. This is convenient for approximating ion densities. This can be done by measuring ion current density along the length of the target for different HAIS currents, and then using the electron temperature

that corresponds to the bias condition of interest. It is also convenient for data collection because the Faraday probe will not be exposed to the sputtering process, which could lead to electrical shorts overtime, as was experienced to be detrimental with near field triple probe measurement attempts.

Figure 6.6a shows ion current and ion density at several discharge currents without applied biases to the target. These data can be used to compare to the actual current collection indicated



(a)



(b)

**Figure 6.6:** Ion current density and ion density along target length for various anode discharge currents. (a) Ion current density and number density over target length for various discharge currents. (b) Ion density along target length.

on the target power supply by integrating the measured ion current density over the inside surface area of the tubular target. The comparison of measured ion current and the indicated ion current collected on the target is shown in Table 6.1 for -300VDC target biases. The measured values are

**Table 6.1:** Indicated and measured ion current to target surface comparison.

Anode Current	Indicated Current [mA]	Measured Current [mA]	Percent Difference (%)
1.0	280	270.9	3.25
1.5	420	389.6	7.24
2.0	580	516.4	10.97
3.0	860	787.3	8.45

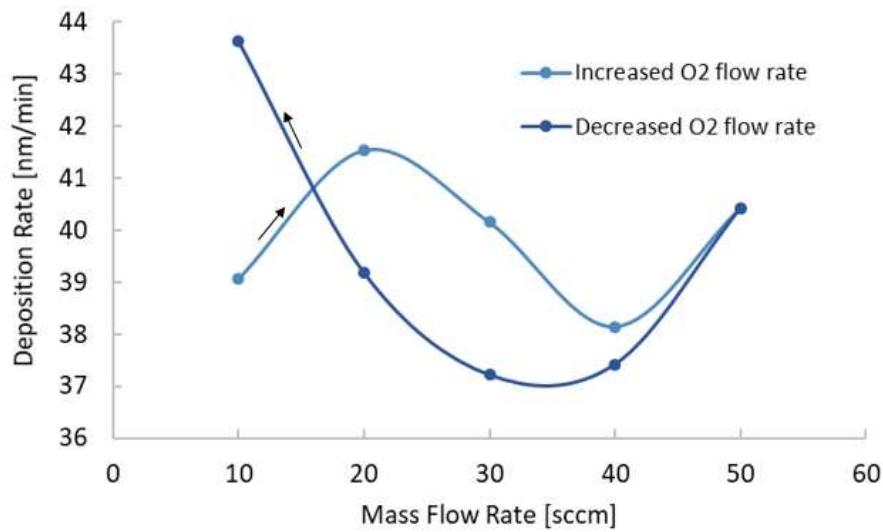
found to be lower than the indicated current reading on the power supply. This can be due to many factors, such as secondary electron emission from the target surface, or losses to photon emission. The Faraday probe was likely to have not been perfectly aligned with the target surface, which could have also played a role in the ion current measurements.

### 6.3 Deposition Rates

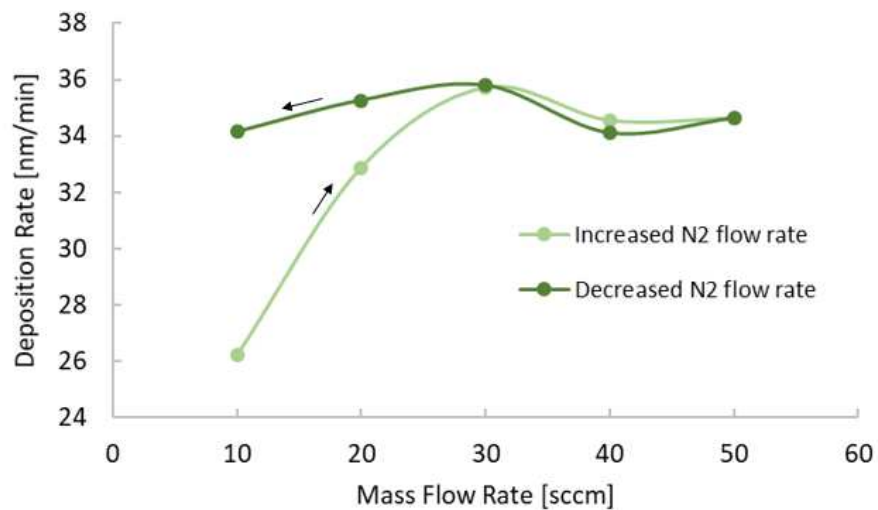
A quartz crystal microbalance (QCM) was used to measure deposition rates of Ti with and without O<sub>2</sub> and N<sub>2</sub> process gases. By measuring deposition rates, the setting with the highest deposition rate and desired profile can be chosen to reduce coating time, as well as gauge the amount of time required for a desired thin film. The experimental set up showing the QCM can be seen in Figure 6.4. The QCM is able to measure deposition rates by sensing changes of an applied frequency due to mass change during deposition. A water chiller was used to maintain a steady cooling temperature of 20°C on the sensor during deposition. This was used to limit measurement errors caused by thermal effects. The densities of bulk materials were used to calculate the approximate deposition rate.

The measurements were taken for various partial pressures of process gases and over lateral distances to provide deposition profiles for the operating conditions of interest. Oxygen and ni-

trogen mass flow rates were varied to measure the resultant deposition rates of the reactive sputter process. Figure 6.7 shows the deposition rate as a function of increasing and decreasing process gas flow rates of O<sub>2</sub> and N<sub>2</sub>. These QCM measurements were taken directly down stream of the deposition source (at a lateral distance of 0cm). It is interesting to note the change in deposition



(a)



(b)

**Figure 6.7:** Deposition rate for -300V target bias at 3.0A anode discharge current at center line for increasing and decreasing process gas flow rate. (a) Oxygen process gas. (b) Nitrogen process gas.

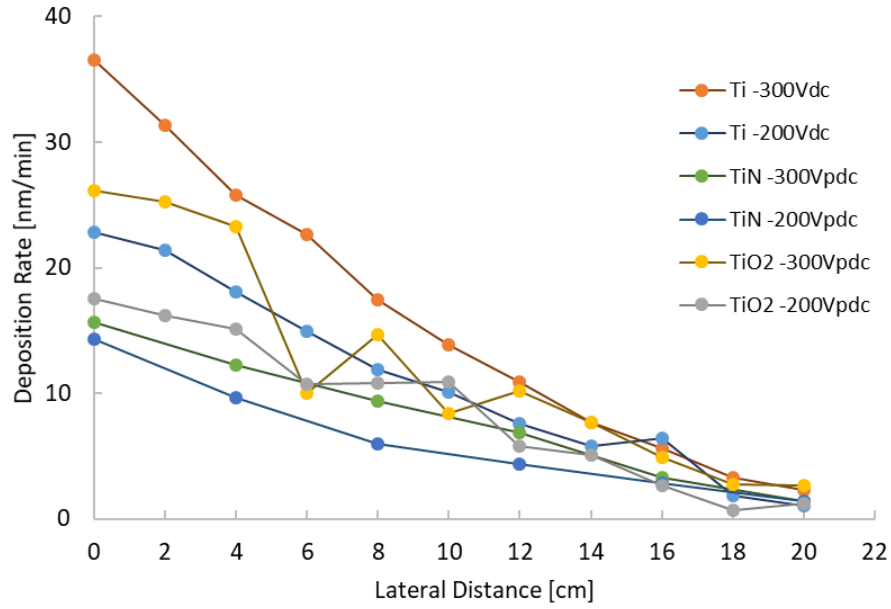
rates for the same mass flow rates, depending on whether the flow is increased or decreased. This

is known as a hysteresis in deposition rate that corresponds to the partial pressure of the reacting process gas. This phenomena is related to different stoichiometric combinations caused by the amount of process gas partial pressure during reactive sputtering [6, 11].

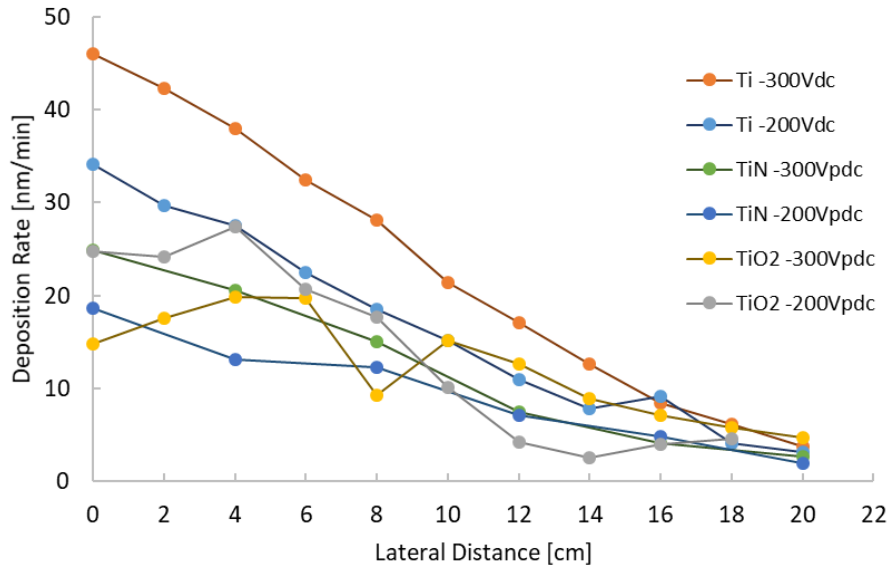
The process used for measuring deposition rates during reactive sputter deposition follows. A bias is applied to the target. After warming the target to ensure contaminants are free from the surface, process gas is slowly introduced. The indicated facility pressure will not change while increasing process gas flow until a reaction threshold is met. Past this point, all of the Ti reacts with the process gas and the excess process gas contributes to the background gas pressure in the vacuum chamber [32]. After this threshold was met, the desired process gas flows were set. Reactive deposition occurred at 30sccm O<sub>2</sub> for TiO<sub>2</sub>, and 20sccm N<sub>2</sub> for TiN. The required mass flow rates for the desired stoichiometric ratios were approximated using flux calculations of Ti deposition rates and process gas flows, as shown in Appendix E. It is assumed that TiO<sub>2</sub> and TiN are grown at these process gas flow rates. Figure 6.8 shows the deposition rate profiles for 2.0A and 3.0A anode discharge currents for Ti, TiO<sub>2</sub>, and TiN at a throw distance of 20cm. Figure 6.8 shows how the deposition rates vary for different discharge currents. The deposition rates corresponding to the partial pressure curves for O<sub>2</sub> and N<sub>2</sub>, shown in Figure 6.7 can be used to approximate a deposition profile by scaling the deposition profiles by a deposition rate corresponding to the mass flow rate of process gas.

Figure 6.9 shows the deposition profile for Ti at a 2.0A anode discharge and a throw distance of 12.5cm. The deposition rate profile is shown to increase for a decreased throw distance. The TiO<sub>2</sub> deposition rates measured downstream of the HAIS orifice at 0cm lateral distances are shown to decrease from the 2.0A discharge to the 3.0A discharge. Figure 6.9 shows how the deposition rates decrease towards the centerline for TiO<sub>2</sub> films growth with a 3.0A anode discharge. This is believed to be due to increased ion assist, or etching, at higher levels of ion production during the deposition process.

It is observed that at -200V to -250V target biases, the current to the target increases by about 20%, and decreases at voltages higher than -250V. This could be due a number of events at the



(a) Deposition rate profile for 2.0A anode discharge current.



(b) Deposition rate profile for 3.0A anode discharge current.

**Figure 6.8:** Deposition profile for various target biases and process gas species at a 20cm throw distance. (a) Deposition rate profile for 2.0A anode discharge current. (b) Deposition rate profile for 3.0A anode discharge current.

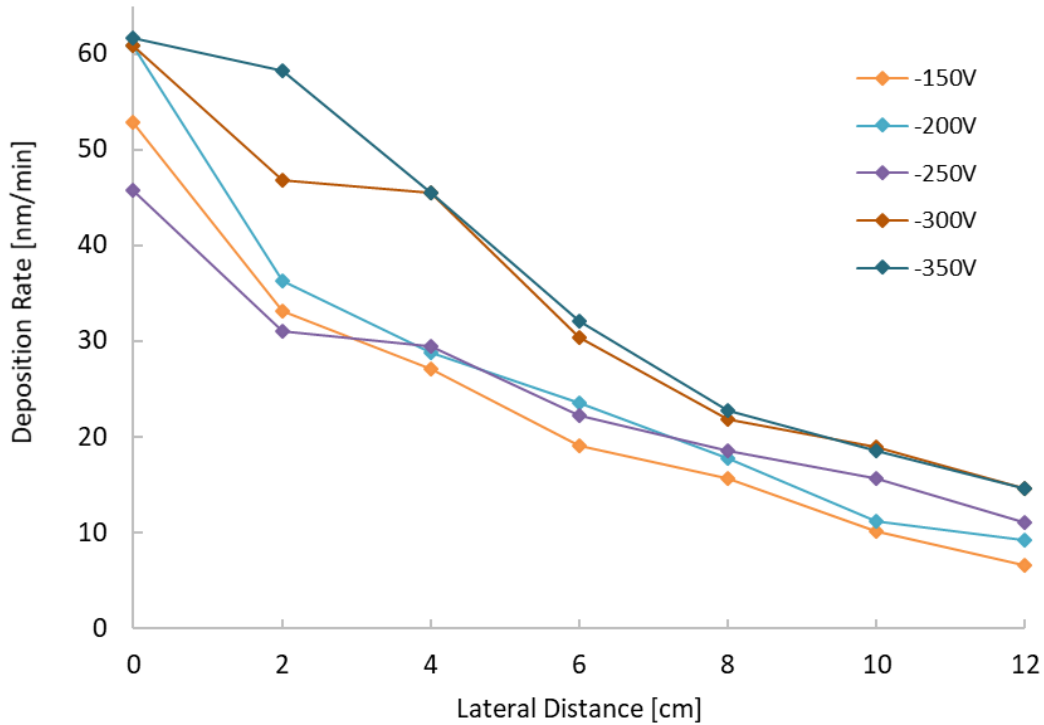


**Figure 6.9:** Deposition profile for various target biases and process gas species at a 12.5cm throw distance.

target surface, as described in Figure 1.4. Ar ions may be bombarding the surface with the right amount of energy to cause an increase in secondary electron emission, which would result in higher current readings on the power supply. At these operating conditions the ion current or deposition rate are not found to increase with the current reading, suggesting that a mechanism other than ion neutralization is participating in the target current at this operating condition. According to a NASA report on the secondary electron emission yields of titanium targets, it is shown that at in the range of 250eV to 300eV, the yield approaches a maximum [33]. This is the energy argon ions fall through when this current increase is observed, suggesting that secondary electron emission may be adding to the indicated current on the power supply. There are likely other factors affecting the current reading that are beyond the scope of this research. These factors could be explored for further characterization of the deposition system.

# Chapter 7

## THIN FILM CHARACTERIZATION

Due to the inherently high energy deposition and ion assist processes used by the system, it can be assumed that thin films of high density and relatively high compressive stress are produced [6, 9, 10]. The index of refraction of several TiO<sub>2</sub> samples were measured to compare to bulk materials to check if this was true. The residual stress was also measured for a sample prepared using a typical deposition process for TiO<sub>2</sub> to verify the assumption.

### 7.1 Ellipsometry

Ellipsometry was used to calculate thin film thicknesses and indices of refraction of thin film samples prepared at several operating conditions. An ellipsometer is an instrument that detects changes in polarized light directed at a surface. Information about the reflected light, such as changes in polarization and energy, are used to measure thin film properties like thickness, reflectance, transmittance, index of refraction, absorption, etc.

TiO<sub>2</sub> thin films deposited on glass for DC and pulsed-DC target biases at 2.0A and 3.0A anode discharge currents were studied using ellipsometry. The index of refraction of thin films prepared by various operating conditions of the HAIS system, thin films prepared by other methods, and bulk crystalline TiO<sub>2</sub> are shown in Figure 7.1. The index of refraction of the thin films are shown to be comparable to that of bulk titanium dioxide. The data also suggest that the refractive index can be increased by increasing deposition energy, hence the density of the film will be increased. This is shown by the shift in refractive index towards bulk values as the target power and anode current are increased. Since the thin films are close to bulk values it can be assumed that the films are being deposited with low porosity, or high density. The effective index of refraction of air gaps within the media would cause a lower measured index of refraction. The level of porosity was estimated using the Lorentz-Lorenz effective medium model, which uses equation (7.1) to calculate porosity [35, 36].

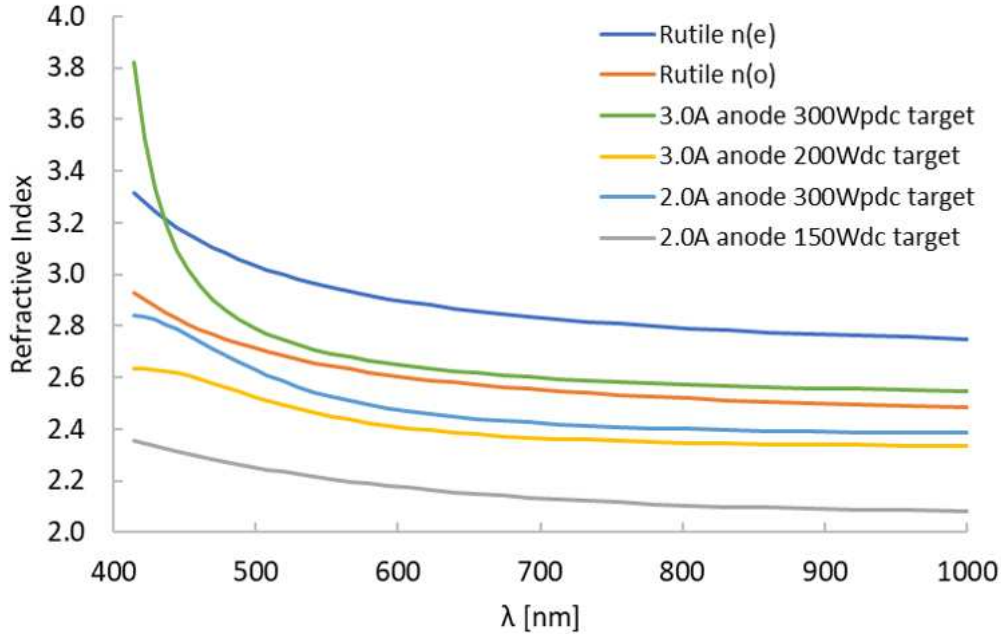


**Figure 7.1:** Bulk rutile TiO<sub>2</sub> refractive index comparison to TiO<sub>2</sub> thin films prepared by HAIS deposition system. Ordinary and extraordinary indices of refraction for rutile TiO<sub>2</sub> were adapted from "Refractive Indices of Rutile and Sphalerite," by J. R. DeVore, 1951, *Journal of the Optical Society of America* 41 (6), p.418. Copyright [1951] by the Journal of the Optical Society of America [34].

$$p = 1 - \left( \frac{n_a^2 - 1}{n_a^2 + 2} \right) \left( \frac{n_{bulk}^2 + 2}{n_{bulk}^2 - 1} \right), \quad (7.1)$$

Where  $n_a$  is the thin film index of refraction, and  $n_{bulk}$  is the bulk index of refraction for TiO<sub>2</sub>. Equation (7.1) is used to find the percent porosity comparison of thin films grown at different deposition conditions by the HAIS system to the ordinary and extraordinary indices of rutile TiO<sub>2</sub>, and TiO<sub>2</sub> thin films grown by reactive thermal evaporation with and without ion assistance.<sup>1</sup> Table 7.1 shows a comparison of the prepared samples with the HAIS deposition system to bulk crystalline TiO<sub>2</sub>, and thin films prepared using thermal evaporation with and without ion assisted deposition (IAD) using (7.1).

The negative percentages in Table 7.1 represent a less porous thin film and a positive percent represents a more porous thin film. The thin films with higher levels of porosity than the bulk

<sup>1</sup>The refractive index of thin films prepared using reactive thermal evaporation was adapted from reference [37]. The refractive index of thermal evaporated thin films prepared with ion assist was adapted from reference [38]. Ordinary and extraordinary indices of refraction for rutile TiO<sub>2</sub> were adapted from reference [34].

**Table 7.1:** Percent porosity comparison for HAIS deposited thin films and other TiO<sub>2</sub> materials.

$n_{\text{HAIS}}(623\text{nm})$	$P_{\text{target}}$ [W]	$J_{\text{anode}}$ [A]	$P_{\text{evapIAD}}(\%)$	$P_{\text{evap}}(\%)$	$P_{\text{ordinary}}(\%)$	$P_{\text{extraordinary}}(\%)$
2.54	156 (DC)	2.0	-9.13	-21.25	1.60	8.97
2.55	174 (DC)	2.0	-9.49	-21.65	1.27	8.67
2.50	300 (10kHz)	2.0	-7.66	-19.62	2.92	10.19
2.50	300 (10kHz)	3.0	-7.66	-19.62	2.92	10.19
2.45	252 (DC)	3.0	-5.76	-17.51	4.63	11.78
2.50	204 (DC)	3.0	-7.66	-19.62	2.92	10.19
2.16	152 (DC)	2.0	6.96	-3.37	16.10	22.39
2.42	174 (DC)	2.0	-4.58	-16.20	5.70	12.76
2.26	300 (10kHz)	2.0	2.22	-8.63	11.83	18.44
2.59	264 (10kHz)	3.0	-10.90	-23.22	0.00	7.49
2.74	294 (10kHz)	3.0	-15.80	-28.66	-4.42	3.40

crystalline material suggests that the films are being deposited in an amorphous structure [37–39]. Thin films prepared by thermal evaporation with and without IAD are shown to be more porous than thin films grown by the sputter system under study. It has been shown by many researchers, and again here, that thermal evaporation with ion assist can improve thin film density and structural properties [37, 40]. The film porosity over almost all deposition conditions grown by sputter deposition are shown to be superior to films grown with thermal evaporation with and without IAD, and close to bulk values at increased deposition energies. Based on the dispersion data received from ellipsometry, the thin films produced by the system are likely dense and in compressive stress.

## 7.2 Residual Stress

Since porosity is directly related to the density, it can also be assumed that the films are being grown in a compressive manner [10]. The residual stress of a TiO<sub>2</sub> thin film deposited on a glass substrate was calculated to verify this assumption. Using the same deposition procedure described in Chapter 6, a TiO<sub>2</sub> thin film was grown with a 3.0A anode discharge, 30sccm O<sub>2</sub> flow and at 300W pulsed-DC sputter deposition. A qualitative understanding of the thin film density can be deduced from the residual stress of the film. The Stoney equation was used to find the residual stress of the film.

$$\sigma_f = \frac{E_s t_s^2}{6(r_f - r_s)(1 - \nu_s)t_f}, \quad (7.2)$$

Where  $r_s$  is the substrate radius of curvature prior to deposition,  $r_f$  is the film radius of curvature,  $E_s$  is the elastic modulus of the substrate,  $\nu_s$  is Poisson's ratio of the substrate,  $t_s$  is the substrate thickness, and  $t_f$  is the thin film thickness.

Poisson's ratio and the elastic modulus are known material properties of the substrate, of 0.2 and 60GPa respectively. The thickness of the substrate was found using a micrometer to be 0.53mm. The thickness of the thin film was found to be 225nm from ellipsometry measurements.

The radius of curvature of the sample before and after deposition was found using carrier frequency interferometry (CFI). A helium-neon (HeNe) laser ( $\lambda = 632.8\text{nm}$ ) was used to measure the fringe pattern caused by the interference of a known, calibrated, carrier frequency and that of the sample's wavefront. A HeNe laser, pumped through a telescope to increase the beam size, was split between a calibrated sample and the substrate under study to generate the interference pattern. A camera was used to detect the interference signal caused by the two wavefronts. The data were then processed by using a fast Fourier transform (FFT), an inverse FFT, and a phase unwrap to calculate the radius of curvature. The interference signal and resultant radius of curvature contour plot are shown in Figure 7.2.

The radius of curvature of the substrate was found to be 94m prior to deposition, and 13.8m post deposition. The residual stress was found to be highly compressive, with a value of -175GPa.

As mentioned in Chapter 1, a common mechanism shown to cause compressive stress is known as atomic peening. It is also well known that thin films in compressive stress due to this mechanism, have a low level of porosity [9]. It is expected that the thin films are compressive due the high energy and momentum based deposition process and ion assist. There is another factor that could cause compressive stress, which is in the case of film impurities. To conclude that the films are compressive due to atomic peening, film composition would need to be examined using techniques such as energy x-ray dispersive spectroscopy (EDS). Factors that commonly contribute to contamination are oxygen, water, or implanted inert gases due to high energy ion bombardment (on the

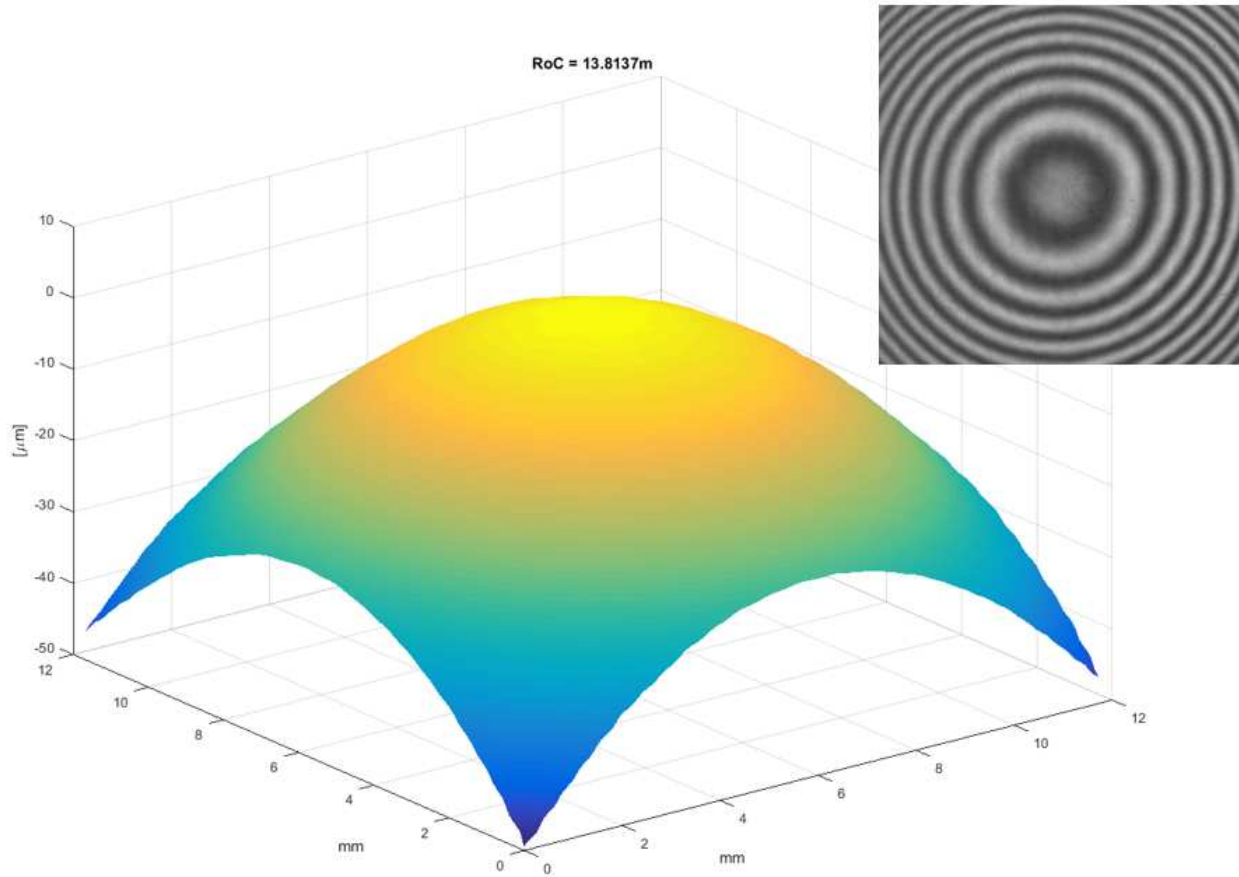


**Figure 7.2:** Radius curvature contour plot of TiO<sub>2</sub> thin film and interference signal (top right) used for residual stress measurement.

order of 1keV) [6,9,10,16]. By using an RGA, the impurities were made sure to be evacuated from the system prior to deposition by reaching a low base pressure and attempting bake out procedures. Also, since energetic particle bombardment occurs at energies lower than the required energy for surface implantation to occur, it is safe to assume that atomic peening is the main mechanism for the observed compressive stress, and does result in thin films of high density.

# Chapter 8

## DISCUSSION

### 8.1 Substrate Cleanliness

Cleanliness is one of the most important, if not the most important factor when working with thin film technologies. Many people in this industry have their own recipes for cleaning, which differ from one place to another. This goes to show that a single solution to the problem has not been found. One thing that has been shown to help with cleaning substrate surfaces is in vacuum by means of ion bombardment [11]. Ion bombardment will be helpful only as a final step for cleaning. Prior to this there should be a series of cleaning steps, which could make use of various solvents, detergents, ultrasound baths, temperature cycling, etc. The following cleaning procedure was used prior to deposition, and was found to provide adequate film adhesion.

First, the glass samples were washed in a dishwasher using standard detergent and approximately one quarter of a cup of vinegar on a high temperature wash and dry setting. Next the substrates were rinsed with isopropyl alcohol and dried using lint free cloths several times. The substrates were then bathed in acetone and dried with nitrogen gas. The previous cleaning steps using isopropyl and acetone were repeated until water spots on the glass were no longer observed after nitrogen drying. The films were then placed in vacuum where the final ion cleaning process was conducted. The ion cleaning involved scanning the HAIS over the substrate at a 3.0A anode discharge current with oxygen background gas introduced at 30sccm near the substrate. The oxygen is believed to react with any of the hydrocarbons that are vaporized from the substrate surface. After the first scan is completed, another cleaning scan is conducted using only argon to provide an inert ion cleaning on the substrate surface. These cleaning processes elevated the temperature of the glass substrates to between 50°C to 100°C, depending on the amount of time the substrate was exposed to the HAIS during cleaning. Adhesion testing was the only form of evaluation for the cleaning process, which was done after the films were deposited. This test was completed by

placing a strip of Kapton tape on the film and pulling it off aggressively. If the tape pulled any of the film off of the substrate then the cleaning procedure used prior to deposition was deemed inadequate. There are several methods for determining cleanliness of a sample, which is described thoroughly in [24].

Steps should also be taken for maintaining a clean vacuum system. By keeping a clean facility the likelihood of film contaminants and pinholes will decrease, leading to increased film quality. Cleaning surfaces free from residual films that eventually flake, as well as using a soft rough to pump, will prevent large contaminants such as flakes and dust from blowing around in the chamber and potentially landing on the substrate surface. These macroscopic flakes cannot be easily removed from the surface during ion cleaning due to their size, and result in film vacancies (pin holes) on the substrate surface.

## **8.2 System Scaling**

The deposition system presented is sufficient for coating substrates with a maximum area of around 0.5m x 1.0 m. This area is currently limited by the travel distances of the linear motion stages. Several components should be considered for a deposition system of larger scale, and also for improving the system's overall performance.

The first component is the motion system. For a larger coating system, more mass needs to be accounted for. This means that an increased load on the motors will be present. Depending on the mass load, motors need to be sized appropriately and linear stages need to be designed accordingly. For the requirement of long travel distances, a lead screw should be avoided to reduce the harmonic vibrations in the system. An alternate solution is to use some sort of belt or chain to drive the linear motion. For a vertical stage to support a more massive deposition system, a stepper motor with a braking mechanism or a gear reduction with enough torque to hold the weight of the system should be used to avoid the system from falling with gravity, which could be detrimental to the system.

To improve the reliability of the system, encoders and motor drivers should be used to account for the system motion. This should be done in a way to ensure that steps will not be missed, and motors will not be damaged from loading the system at a travel limit. To avoid any harmful EMI to limit switches during operation, infrared limit could also be implemented to improve the reliability of the coating system.

## Chapter 9

### CONCLUSION

A sputter deposition proof of concept that uses a novel hidden anode ion source, was turned into a development project after it was found to produce adherent thin films of Ti and TiO<sub>2</sub> on glass and metal substrates. To the author's knowledge, an ion source of this design has not been used in a deposition system before. Compared to commercial deposition systems and ion sources, the rate of ion production of the H AIS are found to be equivalent, the deposition rates have been found to be comparable, and the ion source and system components come to a fraction of the cost of most modern deposition systems due to the simplicity of design. Due to these factors, along with the ability to coat large substrates, the deposition system presented is an excellent candidate for creating large scale art pieces. The ability to produce thin films with low porosity allows for the pieces to be exposed to outdoor environments for a long duration of time.

In the future it would be beneficial to test different target materials and measure deposition profiles. The deposition profiles could then be modeled to predict thickness uniformity and the thickness needed to produce desired results. This could be done by taking into account variables that effect the growth rate, which include scanning velocity, distance between scans, and the power to the target. The deposition model could also take into account ion assist etching during thin film growth. But for now the system is to be used as a tool for visual art, and it is beneficial to approach the deposition process with an experimental attitude to learn what can be produced from different deposition settings. Learning from the outcomes is an important part of the creative process because it breeds new ideas about how the piece can be executed, as well as developing new ways of looking at the thin films.

# Bibliography

- [1] J. E. Greene. Review article: Tracing the recorded history of thin-film sputter deposition: From the 1800s to 2017. *Journal of Vacuum Science Technology*, 2017.
- [2] J. Thirumalai. Introductory chapter: The prominence of thin film science in technological scale, thin film processes - artifacts on surface phenomena and technological facets. <https://www.intechopen.com/books/thin-film-processes-artifacts-on-surface-phenomena-and-technological-facets/introductory-chapter-the-prominence-of-thin-film-science-in-technological-scale>, April 2017.
- [3] D. R. Askeland. *The Science and Engineering of Materials*, volume 7. Cengage Learning, Massachusetts, USA:, 2015.
- [4] G. R. Fowles. *Introduction to Modern Optics*, volume 2. Holt, Rinehart and Winston, Inc. New York, USA:, 1975.
- [5] J Peatross and M. Ware. *Physics of Light and Optics*, volume 1. Brigham Young University, USA:, 2015.
- [6] M. Ohring. *The Materials Science of Thin Films*, volume 1. Academic Press, California, USA:, 1992.
- [7] J. E. Mahan. *Physical Vapor Deposition of Thin Films*, volume 1. John Wiley Sons, Inc., New York, USA:, 2000.
- [8] B. Ning, M. Shamsuzzoha, and M. L. Weaver. Influence of processing variables on the properties of dc magnetron sputtered nial coatings containing hf additions. *Journal of Vacuum Science and Technology A*, 2005.
- [9] H. Windischmann. Intrinsic stress in sputtered thin films. *Journal of Vacuum Science Technology*, 1991.

- [10] H. Windischmann. Intrinsic stress in sputter-deposited thin films. Technical report, DP America R and D.
- [11] L. Holland. *Vacuum Deposition of Thin Films*, volume 6. Chapman and Hall, London, England:, 1966.
- [12] S. Chen and T. Sekiguchi. Instantaneous direct-display system of plasma parameters by means of triple probe. *Journal of Applied Physics*, 1965.
- [13] J. Jeans. *An Introduction to the Kinetic Theory of Gases*, volume 1. Cambridge University Press, London, England:, 1940.
- [14] F. Chen. *Introduction to Plasma Physics and Controlled Fusion*, volume 1. Plenum Press, New York, USA:, 1984.
- [15] L. B. Loeb. *The Kinetic Theory of Gases*, volume 2. McGraw-Hill Company, Inc., New York, USA:, 1934.
- [16] K. Seshan. *Handbook of Thin-Film Deposition Processes and Techniques*, volume 2. Noyes Publications, New York, USA:, 2002.
- [17] P. Sigmund. Theory of sputtering. i. sputtering yield of amorphous and polycrystalline targets. Technical report, Metallurgy Division, Argonne National Laboratory, Argonne, Illinois, 60439, April 1969.
- [18] M. H. Suhail, G. Mohan Rao, and S. Mohan. Dc reactive magnetron sputtering of titanium-structural and optical characterization of tio<sub>2</sub> films. *Journal of Applied Physics*, 1992.
- [19] T. Oya and E. Kusano. Effects of radio-frequency plasma on structure and properties in ti film deposition by dc and pulsed dc magnetron sputtering. *Thin Solid Films*, 2009.
- [20] M. Taborelli. Cleaning and surface properties. Technical report, CERN, CERN, Geneva, Switzerland, ? 2007.

- [21] V. Gorkhovskiy. Teactors for plasma-assisted processes and associated methods, 2019.
- [22] S. Avtaeva, V. Gorokhovskiy, S. Robertson, and E. Shunko. Characterization of low-pressure high-current cascaded arc plasma in large volumes. *Spectrochimica Acta Part B: Atomic Spectroscopy*, 2020.
- [23] C. F. Burns. Critical melting point and reference data for vacuum heat treating. <https://solarmfg.com/wp-content/uploads/2011/01/Critical-Melting-Point1.pdf>, September 2010.
- [24] S. D. Kovaleski, M.J. Patterson, G. C. Soulas, and T. R. Verhey. A review of testing of hollow cathodes for the international space station plasma contactor. Technical report, National Aeronautics and Space Administration, Glenn Research Center, Cleveland, Ohio, 44135, December 2001.
- [25] H. Barankova and L. Bardos. Hollow cathode and hybrid plasma processing. *Vacuum*, 2006.
- [26] A. F. Forzati, W. R. Norris, and F. D. Rossini. Vapor pressures and boiling points of sixty api-nbs hydrocarbons. *U.S. Department of Commerce, National Bureau of Standards*.
- [27] R. K. Ham, J. D. Williams, S. J. Hall, G. F. Benavides, and Verhey. Characterization of propellant flow and bias required to initiate an arc discharge in a heaterless hollow cathode. *AIAA*, 2019.
- [28] R. K. Ham, J. D. Williams, S. J. Hall, G. F. Benavides, and T. R. Verhey. Characterization of a fixed-volume release system for initiating an arc discharge in a heaterless hollow cathode. *IEPC*, 2019.
- [29] A. Qayyum, S. Ahmad, R. Khan, S. Hussain, F. Deeba, M. A. Javed, N. Ahmed, R. Ali, and S. Mehmood. Triple-probe diagnostic measurements in plasma of glast spherical tokamak. *Journal of Fusion Energy*, 2015.
- [30] B. Beal, A. D. Gallimore, and A. W. Hargus. Plasma properties downstream of a low-power hall thruster. *Physics of Plasmas*, 2005.

- [31] D. L. Brown, M. L. R. Walker, J. Szabo, W. Huang, and J. E. Foster. Recommended practice for use of faraday probes in electric propulsion testing. *Journal of Propulsion and Power*, 2017.
- [32] S. Kadlec, J. Musil, and H. Vyskocil. Hysteresis effect in reactive sputtering: A problem of system stability. *Journal of Applied Physics*, 1986.
- [33] A. N. Curren, K. A. Jensen, and G. A. Blackford. Secondary electron emission characteristics of untreated and ion-textured titanium. Technical report, National Aeronautics and Space Administration, Lewis Research Center, Cleveland, Ohio, 44135-3191, March 1989.
- [34] J. R. DeVore. Refractive indices of rutile and sphalerite. *Journal of the Optical Society of America*, 1951.
- [35] C. Millan, C. Santonja, M. Domingo, R. Luna, and A. Satorre. An experimental test for effective medium approximations EMAs porosity determination for ices of astrophysical interest. *Journal of Astronomy and Astrophysics*, 2019.
- [36] M. Laube, F. Rauch, C. Ottermann, O. Anderson, and K. Bange. Density of thin  $\text{TiO}_2$  films. *Nuclear Instruments and Methods in Physics Research Section B: Beam Interactions with Materials and Atoms*, 1996.
- [37] K. Narasimha Rao. Influence of deposition parameters on optical properties of  $\text{TiO}_2$  films. *Society of Photo-Optical Instrumentation Engineers*, 2001.
- [38] M. Gilo and N. Croitoru. Properties of  $\text{TiO}_2$  films prepared by ion-assisted deposition using a gridless end-hall ion source. *Solid Thin Films*, 1996.
- [39] S. Tanemura, L. Miao, P. Jin, K. Kaneko, A. Terai, and N. Nabatova-Gabain. Optical properties of polycrystalline and epitaxial anatase and rutile  $\text{TiO}_2$  thin films by rf magnetron sputtering. *Applied Surface Science*, 2003.

[40] N. K. Sahoo, S. Thakur, D. Bhattacharyya, and N. C. Das. Ion assisted deposition of refractory oxide thin film coatings for improved optical structural properties. March 1999.

# Appendix A

## Alumina Silicate Curing Procedure

Alumina silicate, also known as Lava or Wonderstone, is a machinable ceramic in its 'green' state (prior to curing). The ceramic material is less costly than most other machinable ceramics, such as Maycor, with dielectric properties adequate for the application discussed here. These factors make alumina silicate an excellent material for experimenting with HAIS designs, all at a low cost. A CEPPE Lab procedure used to cure the ceramic material after machining follows.

Lundenburg Furnace:

1. Room temperature to 550°C at 100°C/hr increments

Thermolyne (Programmable High Temp Furnace):

WARNING - Heating elements in furnace are very brittle, do not touch!

1. 0 to 500°C at 75°C/min
2. 500 to 1050°C at 0.2-1.0°C/min (low ramp rate for parts thicker than 0.5")
3. Dwell at 1050°C for 30-45 min (longer maturing time for parts thicker than 0.5")
4. Naturally Cool to Room Temp

Note: Expansion of 1% occurs after firing (i.e. holes expand 1% of original dimension, hole patterns expand 1% of original radial placement)

## Appendix B

### Motion Control Sample Program

```
// Sample Motion Program for Graded Coating
// Ryan Ham and Jack VanGemert
class Motor {
    //pins
    int motor_dir_pin;
    int motor_step_pin;
    int motor_enable_pin;
    int switch_pin;

    long delayTime;
    long stepCount;
    long previousMicros;
    boolean isHomed = false;

public:
    Motor(int Dir, int Step, int Enable, int Switch, long delayMicros){
        motor_dir_pin = Dir;
        motor_step_pin = Step;
        motor_enable_pin = Enable;
        switch_pin = Switch;
        delayTime = delayMicros;

        pinMode(motor_dir_pin, OUTPUT);
        pinMode(motor_step_pin, OUTPUT);
        pinMode(motor_enable_pin, OUTPUT);
        pinMode(switch_pin, INPUT);
        disengageHold();

        stepCount = 0;
    }
};
```

```

    previousMicros = 0;
}

void setDelay(long delayMicros){
    delayTime = delayMicros;
}

void resetHomed(){
    isHomed = false;
    stepCount = 0;
}

long getStepCount(){
    return stepCount;
}

void disengageHold(){
    digitalWrite(motor_enable_pin, HIGH);
}

void engageHold(){
    digitalWrite(motor_enable_pin, LOW);
}

//returns false when step_counter = Pos
boolean Update(long Pos){
    if (stepCount == Pos){
        return false;
    }

    unsigned long currentMicros = micros();

    if (currentMicros - previousMicros >= delayTime){

```

```

previousMicros = currentMicros;
if (!isHomed){
    //homedirection
    stepMotorCW(1-(stepCount%2));
    stepCount++;
    if (stepCount>=2){
        stepCount=0;
    }
    if (digitalRead(switch_pin) == HIGH){
        isHomed = true;
        stepCount = 0;
        stepMotorCW(stepCount%2);
    }
}
else{
    if (stepCount != Pos){
        if (stepCount>Pos){
            stepCount--;
            stepMotorCW(stepCount%2);
        }
        else{
            stepCount++;
            stepMotorCCW(stepCount%2);
        }
    }
}
return true;
}

```

```

void stepMotorCCW(int thisStep){
    //thisStep = abs(thisStep);
    switch (thisStep) {
        case 0:
            digitalWrite(motor_enable_pin, LOW);

```

```

        digitalWrite(motor_dir_pin, HIGH);
        digitalWrite(motor_step_pin, HIGH);
    break;
    case 1:
        digitalWrite(motor_enable_pin, LOW);
        digitalWrite(motor_dir_pin, HIGH);
        digitalWrite(motor_step_pin, LOW);
    break;
}
}
void stepMotorCW(int thisStep){
    switch (thisStep){
        case 0:
            digitalWrite(motor_enable_pin, LOW);
            digitalWrite(motor_dir_pin, LOW);
            digitalWrite(motor_step_pin, HIGH);
        break;
        case 1:
            digitalWrite(motor_enable_pin, LOW);
            digitalWrite(motor_dir_pin, LOW);
            digitalWrite(motor_step_pin, LOW);
        break;
    }
}
};

//x Motor (horizontal scans)
int xStep = 5;
int xDir = 6;
int xEnable = 7;
int xSwitch = 10;

//y Motor (vertical increments between scans)

```

```

int yStep = 2;
int yDir = 3;
int yEnable = 4;
int ySwitch = 9;

Motor xMotor(xDir, xStep, xEnable, xSwitch, 500);
Motor yMotor(yDir, yStep, yEnable, ySwitch, 600);

// all units in cm
long pitch = 1000; // steps per cm
long depRadius = 15; // ~ radius of film deposition
long homeXposition = 4; // dist off x limit switch
long homeYposition = 4; // dist off y limit switch
long substrateLength = 32; // substrate length
long substrateHeight = 32; // substrate height
long deltaY = pitch; // vertical increment between sweeps
long sweepYdistance = substrateHeight*pitch; // total y dist
long sweepXmin = homeXposition*pitch; // place substrate dep
radius from limit switch
long sweepXdistance = (substrateLength+depRadius)*pitch;

void setup(){
  Serial.begin(9600);
  homeY(homeYposition*pitch);
  homeX(homeXposition*pitch);

  for(long y=homeYposition*pitch; y<=sweepYdistance; y+=deltaY){
    goTo(xMotor.getStepCount(), y);
    long sweepDelayTime;
    long sweepNumSteps;
    if(y<=sweepYdistance/2){
      //starts with this coating

```

```

        sweepDelayTime = 2000; //pause between horiz incements
        sweepNumSteps = 20; // number of horiz increments
    }else{
        //halfway begin this coating
        sweepDelayTime = 100;
        sweepNumSteps = 1;
    }
    if (xMotor.getStepCount()>sweepXdistance/2){
        sweepXstepdown(sweepDelayTime,sweepNumSteps);
    }else{
        sweepXstepup(sweepXdistance,sweepDelayTime,sweepNumSteps);
    }
}
}

void loop(){
}

void homeX(long xPos){
    xMotor.resetHomed();
    while (true){
        boolean x = xMotor.Update(xPos);
        if (!x){
            delay(100);
            break;
        }
    }
}

void homeY(long yPos){
    yMotor.resetHomed();
    while (true){
        boolean y = yMotor.Update(yPos);

```

```

    if (!y){
        delay(100);
        break;
    }
}
}

void goTo(long xPos, long yPos){
    while (true){
        if (digitalRead(xSwitch)!=HIGH && digitalRead(ySwitch)!=HIGH){
            boolean x = xMotor.Update(xPos);
            boolean y = yMotor.Update(yPos);
            if (!x && !y){
                break;
            }
        }
    }
}

void sweepXstepup(long sweepXdistance, long sweepDelaytime, long sweepNumsteps){
    for (long i = sweepXmin; i <= sweepXdistance;
        i+=((sweepXdistance-sweepXmin)/sweepNumsteps)){
        goTo(i, yMotor.getStepCount());
        delay(sweepDelaytime);
    }
}

void sweepXstepdown(long sweepDelaytime, long sweepNumsteps){
    //Serial.print("sweepXstepdown");
    long incr = ((xMotor.getStepCount()-sweepXmin)/sweepNumsteps);
    for (long i = xMotor.getStepCount();
        i >= sweepXmin; i-=incr){

```

```
    goTo(i, yMotor.getStepCount());  
    delay(sweepDelaytime);  
  }  
}
```

## Appendix C

### Needle Valve Mass Flow Rate Settings for Argon

The following table provides needle valve flow settings for the hidden anode at several upstream pressures. These values are approximate, and have been found using the methods described in Chapter 5.

Upstream Pressure (psi)	Needle Valve Turns	Mass Flow Rate (sccm Ar)
5	0	4
	1/8	5
	1/4	9
	3/8	12
	1/2	15
	5/8	20
	3/4	27
	7/8	31
	1	35
	1 1/8	40
10	0	7
	1/8	8
	1/4	13
	3/8	20
	1/2	24
	5/8	35
	3/4	41
20	0	12
	1/8	14
	1/4	27
	3/8	33
	1/2	48
40	0	20
	1/8	24
	1/4	30
	3/8	35
	1/2	40

# Appendix D

## Bill of Materials

Presented here is an approximate bill of materials (BOM) that would be expected for someone interested in building the deposition system. This BOM does not include the costs associated with a vacuum facility. For someone with access to a vacuum chamber, and interested in having the capability of coating, it is possible to build a system to fit the dimensions of the facility for a lower cost than most commercial systems.

<b>Item</b>	<b>Source</b>	<b>Quantity</b>	<b>Coat ea.</b>	<b>Cost Total</b>
<b>Electrical Components</b>				
60 ohm Resistor(NHS250)	Mouser	1	\$38.85	\$38.85
15 ohm Resistor(HS300)	Mouser	1	\$51.93	\$51.93
Diode (RURG80100-F085)	Mouser	10	\$4.93	\$49.30
Female Banana Jack	Digikey	10	\$0.72	\$7.20
Male Banana Jack	Digikey	10	\$1.37	\$13.72
19" Electrical Rack	Recycling (used)	1	\$100.00	\$100.00
Nickel Lugs (100 pack)	Del City	1	\$12.50	\$12.50
UHV Electrical Wire (10ft)	Amazon	2	\$13.88	\$27.76
Est. Shipping		1	\$50.14	\$50.14
<b>Power Supplies</b>				
Ion Source Supply	TDK Lambda - Ebay	1	\$800.00	\$800.00
Ignitor Supply	TDK Lambda - Ebay	1	\$800.00	\$800.00
Target Supply	Advanced Energy - CSU	1	\$6,000.00	\$6,000.00
Motion Stage Supply	Eventek - Amazon	1	\$89.99	\$89.99
Est. Shipping		1	\$59.86	\$59.86
<b>Motion System</b>				
Axis 1 (x) (819368022247)	Open Builds	1	\$126.99	\$126.99
Axis 2 (y) (819368022247)	Open Builds	1	\$144.99	\$144.99
Axis 3 (z) (819368022247)	Open Builds	1	\$171.99	\$171.99
Cabling (per ft)	Open Builds	20	\$0.39	\$7.80
Limit Switches (6 pack)	Amazon	1	\$6.99	\$6.99
Microcontroller & Drivers	Sparkfun - Ebay	1	\$52.00	\$52.00
Est. Shipping		1	\$15.88	\$15.88
<b>Gas Feed System</b>				
Compression Fittings	Swagelok	10	\$25.00	\$250.00
Shutoff Valves	Swagelok - Ebay	2	\$30.00	\$60.00
Metering Valves	Swagelok - Ebay	1	\$100.00	\$100.00
Porous Flow Restrictor	Mott	1	\$300.00	\$300.00
1/8" stainless steal tubing	McMaster Carr	2	\$37.15	\$74.30
Argon Gas Cylinder	General Air	1	\$120.00	\$120.00
Inert Gas Regulator	Harris/Matheson	1	\$150.00	\$150.00
Est. Shipping		1	\$18.20	\$18.20
<b>Coater System Hardware</b>				
Titanium Target	TMS Titanium	1	\$83.00	\$83.00
Cathode	Plasma Controls	1	\$270.00	\$270.00
Graphite Components	McMaster Carr	1	\$190.44	\$190.44
Aluminum Components	McMaster Carr	1	\$31.40	\$31.40
Alumina Silicate	McMaster Carr	1	\$200.00	\$200.00
Hardware	Fastenal	1	\$30.00	\$30.00
Est. Shipping		1	\$36.12	\$36.12
			<b>Est. Total</b>	<b>\$10,544.09</b>

# Appendix E

## Flux Calculations for Desired Thin Film

### Stoichiometry

Mathematica was used to approximate mass flow rates of process gases for various stoichiometric compositions for the thin films. This was done by comparing the particle flux to the substrate for the sputtered particles and the reactive gas particles. The deposition rate was used to find the Ti particle flux to the substrate. The process gas partial pressure and average thermal velocity were used to find the reactive gas particle flux. To produce the desired film compositions, the mass flow rate of the process gas was approximated for the different deposition rates produced by the operating conditions. By taking the ratio of the two fluxes, an estimated stoichiometric ratio of the elements can be found.

```
In[136]= ClearAll["Global`*"];
```

# Reactive Sputter Deposition

Target material: titanium

Process gas: oxygen ( $O_2$ )

Flux of Ti:

$$\Gamma_{Ti} = \frac{\rho_{Ti} D}{m_{Ti}}$$

$\rho$  - density [ $kg/m^3$ ]

```
In[137]=  $\rho_{Ti} = 4506$ ;
```

D - deposition rate [m/s]

```
In[138]=  $D_{Ti} = 0.58 * 10^{-9}$ ;
```

m - [kg/#]

```
In[139]= (* take product of amu and molar mass *)
```

```
In[140]=  $m_{Ti} = 47.87 (1.66 * 10^{-27})$ ; (* kg/# of  $SiO_2$  *)
```

```
In[141]=  $\Gamma_{Ti} = \rho_{Ti} D_{Ti} / m_{Ti}$ 
```

```
Out[141]=  $3.28888 * 10^{19}$ 
```

Flux of Ti to substrate:  $1.36 * 10^{20} \frac{\text{particles}}{m^2 s}$

Flux of process gas

$$\Gamma_{N_2} = \frac{1}{4} n_{N_2} v_{th}$$

$n_{O_2}$  - number density [ $\# / m^3$ ]

$$n_{O_2} = \frac{p_{O_2}}{k T}$$

$p_{O_2}$  - Partial pressure of  $O_2$  [Pa] ( $5 * 10^{-5}$  torr  $\rightarrow$   $6.67 * 10^{-3}$  Pa)

T - Temperature [K]

k - Boltzmann Constant  $1.38 * 10^{-23} \frac{J}{K}$

```
In[142]=  $p_{O2} = (101325 / 760) * 2.0 * 10^{-5}$ ;
```

```
In[143]=  $T = 275$ ;
```

```
 $k = 1.38 * 10^{-23}$ ;
```

```
In[144]=  $n_{O2} = \frac{p_{O2}}{k T}$ 
```

```
Out[144]=  $7.02621 * 10^{17}$ 
```

$v_{th}$ - average thermal velocity [m/s]

$$v_{th} = \sqrt{\frac{8kT}{\pi m_{O_2}}}$$

$m_{N_2}$ - [kg/#]

In[140]=  $m_{O_2} = 2 * 16 (1.66 * 10^{-27}) ; (* \text{ kg/\# of } O_2 *)$

In[141]=  $v_{O_2} = \sqrt{\frac{8kT}{\pi m_{O_2}}}$

Out[141]= 426.527

In[142]=  $\Gamma_{O_2} = \frac{1}{4} n_{O_2} v_{O_2}$

Out[142]=  $7.49218 \times 10^{19}$

In[143]=  $\Gamma_{O_2} / \Gamma_{Ti}$

Out[143]= 2.27804

In[144]=  $\% = 10^6 (* \text{ parts per million } *)$

Out[144]=  $2.27804 \times 10^6 (* \text{ parts per million } *)$

## Process gas: nitrogen ( $N_2$ )

Flux of process gas

$$\Gamma_{N_2} = \frac{1}{4} n_{N_2} v_{th}$$

$n_{N_2}$ - number density [##/m<sup>3</sup>]

$$n_{N_2} = \frac{p_{N_2}}{kT}$$

$p_{N_2}$ - Partial pressure of  $N_2$  [Pa]

T - Temperature [K]

k - Boltzmann Constant  $1.38 \times 10^{-23} \frac{J}{K}$

In[151]=  $p_{N_2} = (101325 / 760) * 8.8 * 10^{-6};$

In[152]=  $T = 275;$   
 $k = 1.38 * 10^{-23};$

In[153]=  $n_{N_2} = \frac{p_{N_2}}{kT}$

Out[153]=  $3.09153 \times 10^{17}$

$v_{th}$ - average thermal velocity [m/s]

$$v_{th} = \sqrt{\frac{8kT}{\pi m_{N_2}}}$$

$m_{N_2}$ - [kg/#]

$$\text{In[155]: } mN2 = 28 (1.66 \times 10^{-27}); (* \text{ kg/\# of } N2 *)$$

$$\text{In[156]: } vN2 = \sqrt{\frac{8 k T}{\pi mN2}}$$

$$\text{Out[156]: } 455.977$$

$$\text{In[157]: } \Gamma N2 = \frac{1}{4} nN2 vN2$$

$$\text{Out[157]: } 3.52417 \times 10^{19}$$

$$\text{In[158]: } \Gamma N2 / \Gamma T1$$

$$\text{Out[158]: } 1.07154$$

$$\text{In[159]: } \% \times 10^6 (* \text{ parts per million} *)$$

$$\text{Out[159]: } 1.07154 \times 10^6 (* \text{ parts per million} *)$$

## Process gas : nitrogen ( $N_1$ )

Flux of process gas

$$\Gamma_N = \frac{1}{4} n_N v_{th}$$

$n_{N_2}$  - number density [ $\# / m^3$ ]

$$n_N = \frac{p_N}{k T}$$

$p_N$  - Partial pressure of  $N$  [Pa] ( $5 \times 10^{-8}$  torr  $\rightarrow$   $6.66 \times 10^{-6}$  Pa)

$T$  - Temperature [K]

$k$  - Boltzmann Constant  $1.38 \times 10^{-23} \frac{J}{K}$

$$\text{In[160]: } pN = 6.66 \times 10^{-6};$$

$$\text{In[161]: } T = 275;$$

$$k = 1.38 \times 10^{-23};$$

$$\text{In[162]: } nN = \frac{pN}{k T}$$

$$\text{Out[162]: } 1.75494 \times 10^{15}$$

$v_{th}$  - average thermal velocity [m/s]

$$v_{th} = \sqrt{\frac{8 k T}{\pi m_{N_1}}}$$

$m_{N_2}$  - [kg/#]

$$\text{In[163]: } mN = 14 (1.66 \times 10^{-27}); (* \text{ kg/\# of } N2 *)$$

$$\text{In[164]: } vN = \sqrt{\frac{8 k T}{\pi mN}}$$

$$\text{Out[164]: } 644.849$$

4 | Process Gas Flux Calculator for Reactive Sputter Deposition.nb

$$\#(166) = \Gamma N = \frac{1}{4} n N v N$$

$$\text{Out}[166] = 2.82918 \times 10^{17}$$

$$\#(167) = \Gamma N / \Gamma T i$$

$$\text{Out}[167] = 0.00060226$$

$$\#(168) = \% \times 10^6 \text{ (+ parts per million +)}$$

$$\text{Out}[168] = 8602.26 \text{ (+ parts per million +)}$$